Perlecan Knockdown Significantly Alters Extracellular Matrix Composition and Organization During Cartilage Development

Authors

Alexander R. Ocken, Madeline M. Ku, Tamara L. Kinzer-Ursem, and Sarah Calve

Correspondence

sarah.calve@colorado.edu

In Brief

Perlecan deficiency affects the material properties of developing cartilage. Imaging and proteomic analyses of a murine model of SJS revealed pericellular matrix formation, bulk matrix content and glycosaminoglycan deposition at the articular surface were disrupted. These defects in ECM assembly likely contribute to the reduced matrix integrity that causes improper cartilage development and early onset osteoarthritis seen in SJS.

Graphical Abstract

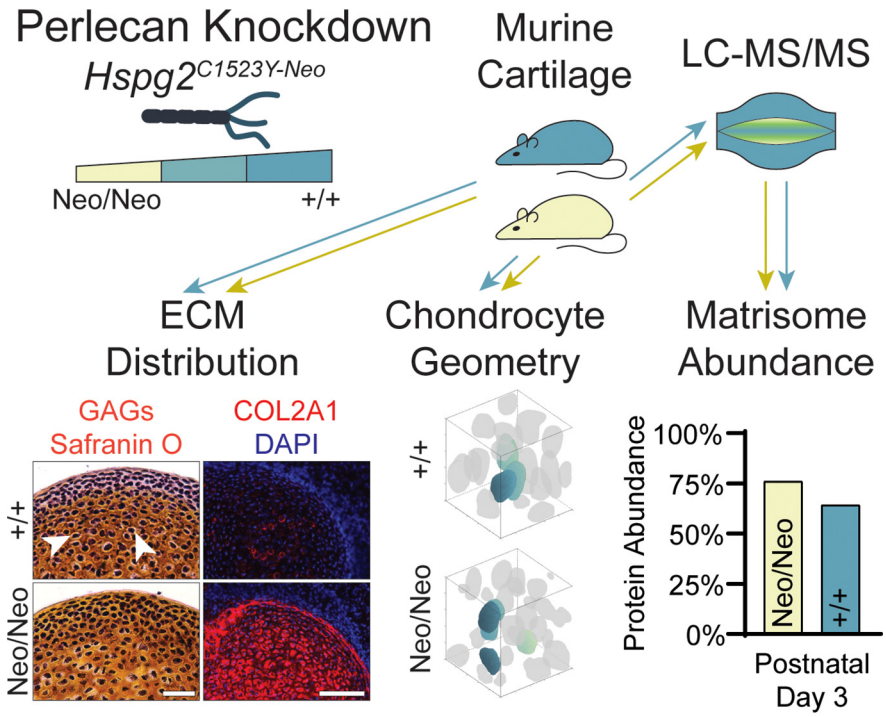

Highlights

- Matrisome content significantly changes with development and perlecan knockdown.
- Chondrocytes respond to perlecan deficiency by increasing bulk matrisome secretion.
- Decreased stiffness may be explained by atypical glycosaminoglycan deposition.
- Elevated COL10A1 expression and chondrocyte hypertrophy indicate early ossification.

Ocken et al., 2020, Mol Cell Proteomics *19(7)*, 1220–1235

https://doi.org/10.1074/mcp.RA120.001998

Perlecan Knockdown Significantly Alters Extracellular Matrix Composition and Organization During Cartilage Development

Alexander R. Ocken, Madeline M. Ku, Tamara L. Kinzer-Ursem, and Sarah Calve*

Perlecan is a critical proteoglycan found in the extracellular matrix (ECM) of cartilage. In healthy cartilage, perlecan regulates cartilage biomechanics and we previously demonstrated perlecan deficiency leads to reduced cellular and ECM stiffness *in vivo*. This change in mechanics may lead to the early onset osteoarthritis seen in disorders resulting from perlecan knockdown such as Schwartz-Jampel syndrome (SJS). To identify how perlecan knockdown affects the material properties of developing cartilage, we used imaging and liquid chromatography-tandem mass spectrometry (LC-MS/MS) to study the ECM in a murine model of SJS, *Hspg2*$^{C1532Y-Neo}$. Perlecan knockdown led to defective pericellular matrix formation, whereas the abundance of bulk ECM proteins, including many collagens, increased. Post-translational modifications and ultrastructure of collagens were not significantly different; however, LC-MS/MS analysis showed more protein was secreted by *Hspg2*$^{C1532Y-Neo}$ cartilage *in vitro*, suggesting that the incorporation of newly synthesized ECM was impaired. In addition, glycosaminoglycan deposition was atypical, which may explain the previously observed decrease in mechanics. Overall, these findings provide insight into the influence of perlecan on functional cartilage assembly and the progression of osteoarthritis in SJS.

The heparan sulfate proteoglycan perlecan is localized to the pericellular matrix (PCM) that surrounds chondrocytes in mature hyaline cartilage. Perlecan is a multifunctional and highly conserved protein known to affect the compressive modulus of the PCM (1, 2) and sequester growth factors (3–5), indicating that it plays a role in both biomechanical and cell signaling. Mutations of the perlecan encoding gene, *Hspg2*, in humans result in defective endochondral ossification and skeletogenesis. Dissegmental dysplasia, Silverman-Handmaker type, is a lethal autosomal recessive disorder that presents with severe chondrodysplasia and dysmorphic facial features because of a null mutation in *Hspg2* (6). Other mutations in *Hspg2* cause the non-lethal Schwartz-Jampel syndrome (SJS), which results in a decreased abundance of functional perlecan and leads to chondrodysplasia, myotonia, and early onset osteoarthritis (7, 8). Although rare, these disorders are difficult to treat, and the therapeutic focus is primarily symptom relief (9).

Murine models generated to elucidate the function of perlecan during development have provided insight into disease progression and mechanisms underlying perlecan deficiency. Global knockout of *Hspg2* in mice is predominantly embryonic lethal, caused by myocardial basement membrane failure under mechanical stress (10). A model with the same point mutation as a form of SJS, *Hspg2*$^{C1532Y-Neo}$, produced mutant mice with similar phenotypes as found in humans, including growth plate defects and myotonia (8, 11). A recent *in vitro* study, which used a fragment of perlecan with a common point mutation found in SJS, found that extracellular signal-regulated kinase (ERK) signaling was disrupted (12). ERK is known to regulate the differentiation of cartilage to bone during development (13), and the presence of intact perlecan may prevent endochondral ossification (12). The absence of functional perlecan in SJS could lead to the activation of ERK signaling and explain why bone differentiation is accelerated. However, because of the multifaceted role of perlecan in regulating signaling within cells through both interactions with the core protein and the sequestration of various growth factors (4, 14), there are likely many additional mechanisms that contribute to the SJS phenotype.

Although studies often focus on the specific genetic mechanisms behind the disorder, a comprehensive profiling of the developing ECM may provide additional insight into how perlecan deficiency affects musculoskeletal functionality. When the initial skeletal template is specified in the embryo, perlecan and other ECM within the cartilage are less organized (15, 16). As chondrogenesis progresses, perlecan and other PCM components (*e.g.* type VI collagen, nidogens) become restricted to the periphery of the chondrocytes, taking on the organization characteristic of adult cartilage ECM. At the same time, chondrocytes increase synthesis of the bulk matrix, which is comprised of type II collagen fibers, glyco-

From the Weldon School of Biomedical Engineering, Purdue University, West Lafayette, Indiana
This article contains supplemental data.
* For correspondence: Sarah Calve, sarah.calve@colorado.edu.
Present address for Sarah Calve: Paul M. Rady Department of Mechanical Engineering, University of Colorado – Boulder, Boulder, Colorado.

DOI 10.1074/mcp.RA120.001998

saminoglycans (GAGs) and proteoglycans, decreasing the overall volume fraction of cells (17, 18). Chondrocytes either maintain the chondrogenic phenotype on the articulating surface to form mature hyaline cartilage or transition to bone within the rest of the skeletal template by first undergoing hypertrophy then endochondral ossification (19). In perlecan-deficient mice, endochondral ossification and PCM formation are disrupted (1, 20). Furthermore, we previously demonstrated that the compressive modulus of both cells and ECM is significantly decreased in the *Hspg2*$^{C1532Y-Neo}$ mouse model (15). Based on these observations, we hypothesized that perlecan knockdown would negatively affect the pericellular incorporation of perlecan binding partners, as well as dysregulate molecules that meditate proper ossification, leading to significant changes in ECM composition.

To test this hypothesis, we first visualized the distribution of key cartilaginous ECM proteins and GAGs in developing cartilage using immunohistochemistry, then assessed the proteome using liquid chromatography-tandem mass spectrometry (LC-MS/MS). We focused our analysis on the ECM proteins, termed the matrisome (21), to better elucidate and compare the composition of healthy and perlecan-deficient cartilage in embryonic and neonatal mice. We found that perlecan knockdown resulted in expected (*e.g.* decrease in PCM components) and unexpected (*e.g.* increase in bulk matrix) trends in ECM abundance. The ultrastructure of the ECM was not significantly different; however, more protein was secreted by *Hspg2*$^{C1532Y-Neo}$ cartilage *in vitro*, suggesting that the ability of newly synthesized ECM to incorporate into the matrix was impaired. Ultimately, perlecan knockdown prevents proper PCM formation and leads to ectopic ossification near the articulating surface (22). These defects in ECM assembly because of perlecan deficiency result in the abnormal cartilage formation and osteoarthritis characteristic of SJS.

EXPERIMENTAL PROCEDURES

All chemicals and reagents were acquired from Sigma-Aldrich (St. Louis, MO) unless otherwise specified

Dissection of Mouse Distal Humeral Cartilage—Mice heterozygous for *Hspg2*$^{C1532Y-Neo}$ (Neo/+) on a DBA background were provided by Dr. Sophie Nicole (Inserm, France) (11) and time mated to generate embryonic day (E)16.5 and postnatal day (P)3 mice. All murine experiments were approved by the Purdue Animal Care and Use Committee (PACUC; protocol 1310000973). Cartilage was dissected from the distal humerus of homozygous (Neo/Neo) and Neo/+ knockdown mice and wildtype (+/+) littermates (Fig. 1*A*). Care was taken to remove ligaments, bone, and ossified cartilage in the epiphyseal plate. Dissected cartilage was rinsed in phosphate-buffered saline (PBS), then immediately processed. Samples were either snap-frozen for proteomic and biochemical assays and stored at −80 °C until used or fixed for transmission electron microscopy (TEM). Tail snips were used to confirm genotypes as previously described (15).

Immunofluorescent Imaging—Forelimbs were embedded in Optimal Cutting Temperature compound (OCT, Sakura Finetek, St, Torrance, CA), frozen in dry ice-cooled isopentane, and stored at −80 °C until sectioned. OCT embedded tissues were sectioned at 17 μm and stored at −20 °C. Before staining, sections were equilibrated to room temperature (RT), rehydrated with 1× PBS for 10 min, fixed with 4% paraformaldehyde (PFA) for 5 min, and rinsed with PBS. Then, sections were permeabilized with 0.1% Triton-X100 (Amresco, Cleveland, OH) in PBS and rinsed with 1× PBS. Background staining was reduced by using the Mouse on Mouse (MOM) staining kit (BMK-2022, Vector Labs, Burlingame, CA). Sections were incubated with MOM IG blocking buffer for 1 h and washed 3 × 2 min with PBS. Sections were primed with MOM protein diluent for 5 min before incubating with primary antibodies overnight and washed 3 × 2 min with PBS. Primary antibodies against COL10A1 (1:50, X53 14-9771-80, Invitrogen, Carlsbad, CA), NID2 (1:50, sc-377424, Santa Cruz Biotechnology, Santa Cruz, CA), HSPG2 (1:50, A7L6 sc-33707, Santa Cruz Biotechnology), type I collagen (1:100, AB765P, Millipore, Burlington, MA) and COL2A1 (1:100, MAB8887, Millipore) were diluted in MOM protein diluent. Biotinylated HABP (385911, Millipore) was diluted 1:150 in MOM protein diluent. Sections were primed again with MOM protein diluent for 5 min before staining with the appropriate secondary detection reagents [Goat anti-mouse IgG1 633 (1:500, Thermo Fisher Scientific, Rockford, IL), Goat anti-mouse IgG1 546 (1:500, Thermo Fisher Scientific), Donkey anti-Rat IgG 488 (1:500, Thermo Fisher Scientific), Donkey Anti-Rabbit 647 (1:500, Thermo Fisher Scientific), Goat Anti-Mouse 546 (1:500, Thermo Fisher Scientific), phalloidin 555 (1:200, Thermo Fisher Scientific), Streptavidin 488 (1:500, Thermo Fisher Scientific), 4′,6-diamidino-2-phenylindole (DAPI, 1:500, Roche, Fishers, IN)] in MOM protein diluent for 30 min in the dark. Incubations occurred at RT unless otherwise stated. Sections were mounted with Fluoromount-G (Electron Microscopy Sciences, Hatfield, PA) and imaged at 10× and 20× using a DMI6000 inverted microscope (Leica, Buffalo Grove, IL). The same acquisition parameters were used for all samples and images were processed using FIJI (23, 24).

Dimethylmethylene Blue (DMB) Assay—Glycosaminoglycans (GAGs) were extracted from distal humeral cartilage using a guanidine extraction buffer. Briefly, snap-frozen cartilage from right and left humeri was pooled (~1.5 and 2 mg wet-weight tissue from E16.5 and P3 cartilage, respectively) and pulverized using a tissue homogenizer (Ace Glass, 8325–08, Vineland, NJ) sitting in a liquid nitrogen bath. Pulverized samples were placed on ice for 15 min to allow the temperature to equilibrate. Samples were resuspended in 1 ml guanidine extraction buffer (4 M guanidine HCl, 50 mM sodium acetate, 100 mM N-ethylmaleimide, pH 5.8) by douncing twenty times with the homogenizer, transferred into 1.7 ml MaxyClear microtubes (Axygen, Union City, CA). Sulfated-GAGs were assayed following (25). Briefly, 250 μl of DMB solution (40 mM DMB, 40 mM NaCl, 40 mM Glycine, pH 3.00, 20 μm filtered) was added to 10 μl samples and 10 μl 1× PBS with 1 mM ethylenediaminetetraacetic acid (PBE). Chondroitin 6-sulfate (shark cartilage, C4384) in PBE was used as a standard, adding 250 μl of DMB solution to 10 μl standards and 10 μl guanidine extraction buffer. Optical density was measured at 530 and 590 nm, where the 590-baseline peak was subtracted from the 530 nm signal to increase assay sensitivity.

Safranin O Staining—PFA fixed cryosections were stained with Harris' hematoxylin (Electron Microscopy Sciences) containing 4% glacial acetic acid (v/v) for 5 min, rinsed under tap water, and washed with PBS 2 × 10 min. Sections were stained with safranin O solution (0.1% safranin O w/v in H_2O, 0.22 μm pore vacuum filtered, Polysciences Inc., Warrington, PA) for 5 min, rinsed under tap water, and washed with PBS 3 × 10 min. Sections were mounted with Permount mounting medium (Electron Microscopy Sciences) and imaged at 10× and 20× using a DMI6000 inverted microscope.

Protein and Peptide Sample Preparation and Q-Exactive Tandem Mass Spectrometry—Protein was extracted from snap-frozen cartilage following (26). Samples resuspended in guanidine extraction

buffer were incubated 24 h on a rocking platform at 4 °C and then reduced with 4 mM dithiothreitol for 30 min on an orbital shaker at 56 °C and alkylated with 16 mM iodoacetamide for 1 h in the dark at RT. Extracts were ethanol precipitated (9:1 ethanol/extract) overnight on a rocking platform at 4 °C, followed by centrifugation at 13,750 × *g* for 30 min at 4 °C. Pellets were washed with cold ethanol for 4 h at −20 °C and dried under vacuum. Extracts were resuspended in 500 μl digestion buffer (100 mM Tris base, 2 mM calcium chloride, 10% acetonitrile v/v, pH 8.0), transferred to tissue homogenizers on ice, dounced twenty times, and returned to 1.7 ml microtubes.

Trypsin digestion was performed with 2.5 μg MS grade trypsin (Thermo Fisher Scientific) per mg wet-weight tissue for 16 h on an orbital shaker at 37 °C. Peptides were acidified with 1% trifluoroacetic acid (v/v) and ultra-filtrated using Ultra-micro C-18 SpinColumns (The Nest Group, Southboro, MA) according to the manufacturer's instructions. The eluent was dried using a CentriVap vacuum concentrator (Labconoco, Kansas City, MO) at 45 °C and resuspended in 10 μl running buffer (3% acetonitrile, 0.1% formic acid v/v). Peptide concentration was measured by 205 nm peptide absorbance using a NanoDrop 2000 spectrophotometer (Thermo Fisher Scientific) according to manufacturer's instructions and normalized to 0.2 mg/ml.

Trypsin-digested peptides equivalent to 1 μg were analyzed with a Dionex UltiMate 3000 RSLC Nano System coupled to a Q Exactive™ HF Hybrid Quadrupole-Orbitrap Mass Spectrometer (Thermo Fisher Scientific). Primary spectra were collected from 400 to 1600 *m/z* at 120,000 resolution, a maximum injection time of 100 ms, and a dynamic exclusion of 15 s. The top 20 precursors were fragmented using higher-energy C-trap dissociation at a normalized collision energy of 27%. Tandem spectra were acquired in the Orbitrap at a resolution of 15,000 with a maximum injection time of 20 ms. Xcalibur RAW files were processed by MaxQuant (version 1.6.1.0) (27) to align primary spectra, identify proteins, and calculate relative protein abundance for LFQ. Tandem spectra were searched against the complete *Mus musculus* reference database (ID 000000589, downloaded from UniProt on 04/06/2018) comprising 53,127 proteins and a contaminants database. MaxQuant search parameters are tabulated in supplemental Table S1. Carbamidomethylation was defined as a fixed modification and variable modifications included oxidation of methionine, deamidation of asparagine, and hydroxylation of proline and lysine (28). Initial precursor mass tolerances were set to 20 ppm in the first search and 4.5 ppm in the main search, and fragment mass tolerances were set to 20 ppm. Enzyme cleavage was set to trypsin, allowing for cleavage before proline residues and for a maximum of two missed cleavages. Results were manually filtered, removing contaminants and proteins identified with only modified peptides or by reverse database matching, and requiring a minimum of two razor and unique peptides across all sample replicates for identification and quantification. Raw data sets are available in the MassIVE repository (29).

Biological Process Gene Ontology Analysis—Gene Ontology (GO) analysis was conducted for each pairwise comparison of interest (+/+: E16.5 *versus* P3, E16.5: Neo/Neo *versus* +/+, and P3: Neo/Neo *versus* +/+). All proteins identified in a sample were used to query g:GOSt, the functional enrichment analysis of the g:Profiler web server (30). Leading protein gene names were submitted, specifying organism as *Mus musculus*, statistical domain scope to only annotated genes, and significance thresholding by g:SCS ($\alpha = 0.05$). Positive identification of biological process terms required a minimum of three protein gene names.

Hydroxyproline Assay and Modification Analysis—Hydroxyproline (Hyp) was assayed from snap-frozen cartilage. Both humeri were pooled, dried at 110 °C for 48 h, and weighed on a microbalance (~80 and 110 μg dry-weight tissue from E16.5 and P3 cartilage, respectively). Hyp content was assessed using a Hyp assay kit (MAK008) according to the manufacturer's instructions. Water and HCl were added to maintain dry-weight tissue concentration at 4 μg/μl (water or HCl).

Hyp and hydroxylysine (Hyl) levels were also analyzed by including as variable modifications in MaxQuant. Analyses of hydroxylation were calculated from the MaxQuant evidence table outputs. Raw intensity (**XIC**) of each evidence (*e*) was multiplied by the number of modified residues ($m_{Mod,e}$) for a given modification, either Hyp or Hyl (*Mod*). These values were summed for each experiment (*i*). The summation was multiplied by the LFQ normalization coefficient (N_i) to give the normalized LFQ abundance of a modification for a given sample, $I_{Mod,LFQ,i}$ (Eq. 1).

$$I_{Mod,LFQ,i} = \sum_{e,i}(m_{Mod,e} * \mathbf{XIC}_e) * N_i \quad (1)$$

Next, the number of prolines or lysines modified in each sample was calculated, using the ratio of modified to the total number of residues to calculate relative abundance. First, the number of modified residues ($m_{Mod,e}$) was divided by the total number of residues ($n_{Res,e}$) for a given modification; either Hyp and proline or Hyl and lysine (*Res*). This ratio was multiplied by the raw intensity of each evidence. These values were summed for each experiment to yield the relative intensity of modified to all residues, $I_{Mod,i}$ (Eq. 2).

$$I_{Mod,i} = \sum_{e,i}\left(\frac{m_{Mod,e}}{n_{Res,e}} * \mathbf{XIC}_e\right) \quad (2)$$

Similarly, the relative intensity of unmodified to all residues was calculated $I_{Unmod,i}$ (Eq. 3). In this case, one minus the ratio of modified to total residues was multiplied by each evidence raw intensity. This value was summed for each experiment.

$$I_{Unmod,i} = \sum_{e,i}\left(\left(1 - \frac{m_{Mod,e}}{n_{Res,e}}\right) * \mathbf{XIC}_e\right) \quad (3)$$

Finally, the relative intensity of modified residues was divided by the total relative intensity of all residues and multiplied by the LFQ normalization coefficient (N_i) to give the LFQ normalized percent of modified residues for a given sample, $R_{Mod,LFQ,i}$ (Eq. 4).

$$R_{Mod,LFQ,i} = \frac{I_{Mod,i}}{I_{Mod,i} + I_{Unmod,i}} * N_i \quad (4)$$

Cartilage Sample Preparation and Transmission Electron Microscopy—Freshly dissected cartilage samples were fixed in 2% PFA and 2% glutaraldehyde in 0.1 M cacodylate buffer overnight at 4 °C. Fixed samples were rinsed with cacodylate buffer (3 × 5 min), impregnated with 1% osmium 0.8% ferricyanide for 1 h, rinsed in water (3 × 5 min), stained with 2% aqueous uranyl acetate for 30 min, and rinsed again with water (3 × 5 min). Samples were then ethanol dehydrated (50, 70, 95, 100% sequentially for 1 × 30, 1 × 30, 1 × 30, and 3 × 15 min, respectively) and transitioned to acetonitrile (2 × 15 min) before infiltration with Embed 812 (Electron Microscopy Sciences) and acetonitrile (2:1) for 2 h, (1:2) rotating overnight, and resin for 3 h rotating. Samples were embedded in flat molds and cured overnight at 70 °C in fresh resin. Ultrathin sections were cut at 85 nm with a 45-degree diamond knife (Diatome, Hatfield, PA) on a UC6 ultramicrotome (Leica) and collected on 100 mesh formvar-coated copper grids and post stained in 4% aqueous uranyl acetate and 2% aqueous lead citrate. Sections were imaged on a FEI T12 80kV TEM (FEI Company, Hillsboro, OR) in the Purdue Life Science Microscopy core facility.

Fibril Area Fraction and Fibril Diameter Measurements—Fibril area fraction and diameter measurement protocols were adapted from (31). For fibril area fraction measurements, uniform interstitial matrix

regions between chondrocytes of the distal humeral cartilage were imaged at 30,000×. Three regions of interest (ROI) for both Neo/Neo and +/+ samples were segmented from each of $n = 4$ biological replicates using FIJI. The top layer of cells from the articular surface was excluded so that ROIs included only subsurface ultrastructure to avoid surface irregularities. The mean intensity of the ROI was divided by the maximum intensity range value (256) to calculate the fibril area fraction percentage.

For fibril diameter measurements, uniform interstitial matrix regions were imaged at 120,000× magnification. ROIs were thresholded at the mean intensity. Individual fibrils, oriented transversely, were manually fitted with the ellipse tool. The minor diameter was measured as the fibril diameter. Results for both fibril area fractions and fibril diameters were averaged over the nine ROIs and reported as the average of the $n = 4$ biological replicates ± standard deviation.

Ex Vivo Cartilage Culture and Secretome Protein Preparation—Cartilage was cultured *ex vivo* following (32). Briefly, freshly dissected cartilage samples were washed in 70% ethanol and rinsed in PBS before being cultured in 0.5 ml serum-free, high glucose, HEPES-buffered Dulbecco's modified Eagle's medium with GlutaMAX (Thermo Fisher Scientific), 50 mg/L 2-phospho-L-ascorbic trisodium salt, and 1% antibiotic/antimycotic. The supernatant from each culture was collected once after 48 h and again at the end of 96 h. At the end of the culture period, both the supernatant and cartilage samples were harvested separately and stored at −80 °C until processed for liquid chromatography-tandem mass spectrometry (LC-MS/MS).

The two aliquots of media were combined, precipitated with methanol-chloroform, resuspended in 500 μl digestion buffer by douncing with a tissue homogenizer. Cartilage proteins were extracted as described above, whereas proteins in the supernatant were only reduced and alkylated. Then both sets of proteins were trypsin digested and analyzed by LC-MS/MS as described above. Peptide concentrations were assayed after resuspension in running buffer with a Pierce Quantitative Colorimetric Peptide assay (Thermo Fisher Scientific). Raw data sets are available in the MassIVE repository (33).

Cartilage Tissue Decellularization, Imaging, and Processing—Dissected humeri were decellularized in 0.05% sodium dodecyl sulfate (SDS) in PBS at RT with gentle rocking for 7 d (18). The SDS solution was replaced every 24 h. Post-decellularization, samples were washed 3 × 30 min in PBS at RT and fixed in 4% PFA for 24 h at 4 °C with gentle rocking. Samples were rinsed in PBS overnight at 4 °C and transferred to fresh PBS for storage at 4 °C until stained. Samples were incubated in blocking buffer [10% donkey serum (Lampire, Pipersville, PA) in PBS with 0.1% Triton X-100 (PBST)] for 24 h at 4 °C with gentle rocking. Samples were stained with 20 μg/ml AlexaFluor488-tagged wheat germ agglutinin (WGA) (Thermo Fisher Scientific) diluted in blocking buffer for 48 h at 4 °C with gentle rocking. Samples were washed 2 × 1 h with PBST at RT, then overnight at 4 °C. Finally, samples were rinsed in PBS at 4 °C for 1 h and transferred to fresh PBS for storage at 4 °C until imaged.

Tissue samples were imaged using a 63× oil-immersion plan-apochromat objective (NA = 1.4) on an LSM880 confocal microscope (Carl Zeiss, Oberkochen. Germany). Image stacks were acquired at 1024 × 1024 pixels, 2× line averaged, with 0.22 μm/pixel *xy*-resolution and 0.75 or 0.39 μm *z* axis intervals. The same image acquisition parameters were used for all samples. Three ROIs for both Neo/Neo and +/+ samples were segmented with the same dimensions (28.55 × 28.55 × 28.50 μm, $x \times y \times z$) from each of $n = 3$ biological replicates using FIJI. The top layer of cells from the articular surface was excluded so that ROIs included only subsurface cellular geometries to avoid surface irregularities and provide a consistent volume for comparison.

To calculate cartilage cell volumes and matrix volume fraction, a custom, automated ROI processing and segmentation algorithm developed in MATLAB to construct three-dimensional geometric models was used (18). In brief, the algorithm-processed image stacks were enhanced using median filtering, histogram corrected to improve cell to ECM contrast, followed by adaptive thresholding (Otsu's method), morphological filtering, Chan-Vese active contours, and watershed distance transform to segment cells from the rest of the volume. The resultant binary masks were used to calculate cell and matrix volume fractions.

Finite Element Analysis—To analyze the effect of developing cartilage mechanical properties and geometry, simulated compression was applied to three-dimensional ROIs using ANSYS version 19.0 (ANSYS, Inc., Canonsburg, PA) following (18). Contact between cells and ECM geometries were bonded, and meshes for the finite element analysis had between 170,076 and −248,604 nodes and 99,688–146,073 elements with an average of 216,757 nodes and 127,610 elements per simulation. Cell and ECM compressive moduli were derived from atomic force microscopy (AFM) measurements of viable cartilage previously reported by (15). Poisson's ratios of 0.4 and 0.45 were applied to cells and ECM, respectively (34, 35). Samples were compressed 5% tangential to the articulating surface toward the center of the cartilage. Equivalent von Mises stress and strain were measured for ECM and chondrocytes that were at least 1 μm from the ROI boundary.

Experimental Design and Statistical Rationale—Cartilage LC-MS/MS experiments were conducted on $n = 3$ biological replicates for three genotypes (Neo/Neo, Neo/+, and +/+) and two timepoints (E16.5 and P3). Data were analyzed using SAS 9.4 (SAS Institute, Cary, NC) to evaluate the effect of development (one-way ANOVA) and perlecan knockdown (two-way ANOVA and post-hoc Tukey-adjusted simple effects multiple comparison test) using $\log_2$-transformed LFQ intensities ($\alpha = 0.05$). One-way ANOVA was used when missing data prevented use of two-way ANOVA. Imputation, replacing missing data points with substituted values, may identify differentially expressed proteins that are in low abundance, but will negatively affect the statistical analysis of more highly abundant proteins (36). Two-tailed Student's *t* test was used when missing data prevented use of one-way ANOVA. This method was employed to incorporate degrees of freedom from all experimental groups when considering pairwise comparisons of interest (+/+: E16.5 *versus* P3, E16.5: Neo/Neo *versus* +/+, and P3: Neo/Neo *versus* +/+). Volcano plots were used to visualize the overall change in ECM composition between two specific data sets (*e.g.* E16.5 *versus* P3 for +/+; Neo/Neo *versus* +/+ for E16.5; supplemental Fig. S3), and a false discovery rate (FDR) of 1% was applied to control false positives for multiple tests (37) using Prism 8.0.1 (GraphPad Software, La Jolla, CA).

Ex vivo explant LC-MS/MS experiments were conducted on $n = 3$ or 4 biological replicates for two genotypes (Neo/Neo and +/+) and two experimental conditions (secretome and residual cartilage). Data were analyzed in Prism to evaluate the effect of perlecan knockdown (2-tailed Student's *t* test) using $\log_2$-transformed values ($\alpha = 0.05$). Values were calculated by dividing the LFQ intensity by the summed total intensity for each sample. Results were reported as an average of at least two biological replicates ($n = 3$). Similarly, volcano plots were used to visualize the change in ECM composition and Prism was used to apply 1% FDR (supplemental Fig. S7).

RESULTS

The Distribution of Nidogen-2 and Type X Collagen were Altered in a Murine Model of SJS—To determine how perlecan knockdown influences the ECM composition of cartilage, we analyzed the distal humerus of postnatal-day (P)3 mice, a period

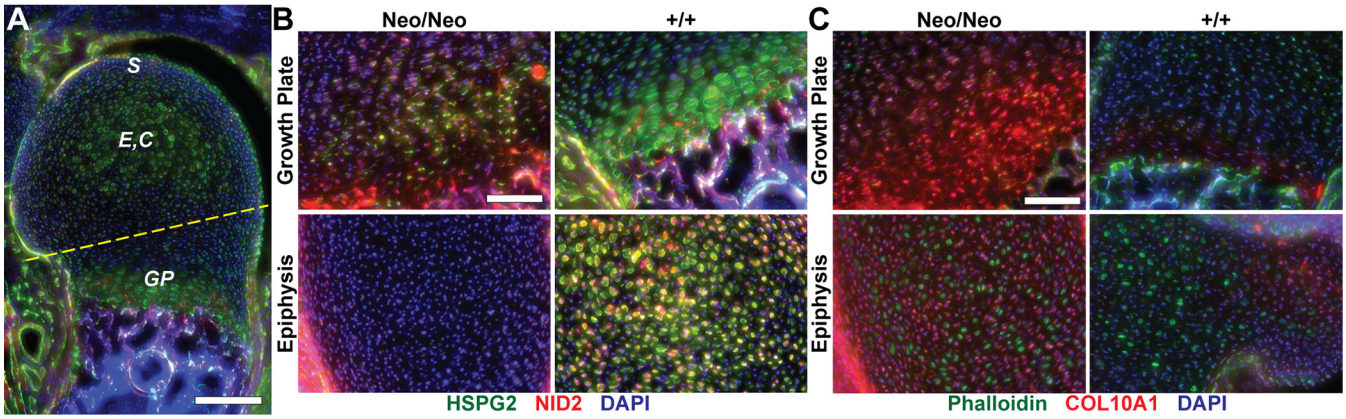

FIG. 1. **Nidogen-2 and type X collagen expression are altered in perlecan-deficient mice.** Immunofluorescent staining of P3 cartilage from the distal humerus. *A*, Perlecan (green) staining in +/+ cartilage. The yellow dashed line indicates the dissection plane for biochemical and LC-MS/MS experiments. *S*: articular surface, *E*: epiphysis, *C*: center, *GP*: growth plate. *B*, Perlecan (HSPG2; green) and nidogen-2 (NID2; red) staining was decreased in Neo/Neo growth plates and epiphyses. *C*, There was an increase in type X collagen (COL10A1; red) in the growth plate and epiphysis of Neo/Neo mice compared with +/+ littermates, whereas there was no difference in actin organization as indicated by phalloidin staining (green). Nuclei were stained with DAPI (blue). Scale bars: (*A*) 200 μm, (*B*, *C*) 100 μm. Images representative of $n = 3$ biological replicates.

that captures the formation of distinct pericellular and bulk (or interstitial) matrices (15). We used the *Hspg2*$^{C1532Y-Neo}$ murine model in which perlecan secretion is reduced, leading to defects consistent with clinical manifestations of human SJS such as muscle stiffness and chondrodysplasia (8, 11). First, to visualize how the organization of key ECM change, cryosections of P3 distal humeri were immunostained for nidogen-2 (NID2), a component of the PCM that binds with perlecan (5, 38), and type X collagen (COL10A1), a protein synthesized by hypertrophic chondrocytes (39). The intensity of NID2 staining was lower in P3 homozygous (Neo/Neo) *Hspg2*$^{C1532Y-Neo}$ mice compared with wildtype (+/+) mice in the epiphysis of the distal humerus (Figs. 1*A*, *B*, supplemental Fig. S1). Like previous studies, NID2 was expressed within the pericellular regions of the epiphysis of +/+ cartilage (Fig. 1*B*) (40). COL10A1 immunolocalization was increased in both the growth plate and epiphysis of Neo/Neo compared with +/+ littermates (Figs. 1*C*, supplemental Fig. S1).

Perlecan Knockdown Affected GAG Deposition at the Articular Surface of Cartilage—Combined with the observation that perlecan knockdown dysregulated ECM proteins crucial for proper cartilage development (Fig. 1) and previous reports that GAG deposition was increased in the intervertebral discs in *Hspg2* exon-3 null mice (41), we investigated whether the *Hspg2*$^{C1532Y-Neo}$ mutation altered GAG abundance in hyaline cartilage. Cartilage was dissected from the distal humeri of P3 +/+ and Neo/Neo mice, taking care to remove the growth plate (Fig. 1*A*). A dimethylmethylene blue (DMB) colorimetric assay, which quantifies sulfated GAG (sGAG) abundance, indicated no significant difference as a function of genotype (Fig. 2*A*). To confirm our biochemical results, we visualized the spatial distribution of GAGs with safranin O counterstained with hematoxylin. Surprisingly, the intensity of safranin O staining at the articulating surface of the cartilage varied between genotypes. For Neo/Neo mice, safranin O distribution was homogenous, decreasing only slightly near the articulating surface (Fig. 2*B*). In contrast, safranin O staining greatly diminished at the articulating surface of +/+ cartilage and the PCM surrounding individual chondrocytes was more pronounced compared with Neo/Neo mice (arrowheads, Fig. 2*B*). Although the DMB assay specifically measures sGAG abundance, we hypothesized that the non-sulfated GAG hyaluronic acid (HA) was responsible for the profile revealed by safranin O, which stains all GAGs. Biotinylated-hyaluronic binding protein (HABP) was used to visualize HA in the tissue and revealed a difference in the distribution between Neo/Neo and +/+ samples. Specifically, HA was ubiquitously found in Neo/Neo cartilage whereas it was decreased at the articulating surface in +/+ animals (Fig. 2*C*). We also evaluated the expression of type II collagen (COL2A1), the major fibril forming collagen in cartilage, revealing elevated levels in perlecan-deficient mice (Fig. 2*C*). Overall, these histological data indicate that different components of both the PCM and bulk ECM were disrupted because of perlecan knockdown.

Matrisome Composition Was Disrupted in Perlecan-deficient Cartilage—To determine how overall ECM protein, or matrisome, composition was affected by perlecan knockdown, we used LC-MS/MS to analyze the distal humeri of embryonic-day (E)16.5 and P3 +/+, heterozygous (Neo/+), Neo/Neo mice. E16.5 captures the developmental period prior to PCM condensation (15). Samples from both forelimbs were pooled and physically disrupted in a chaotropic buffer (4 M GuHCl). Then proteins were extracted, digested into peptides and analyzed by LC-MS/MS (supplemental Fig. S2). Between 59–74 matrisome components were identified in each sample (Fig. 3*A*; supplemental Table S1). The raw intensities of proteins within experimental groups were normalized using label-free quantification (LFQ) in MaxQuant to enable comparison

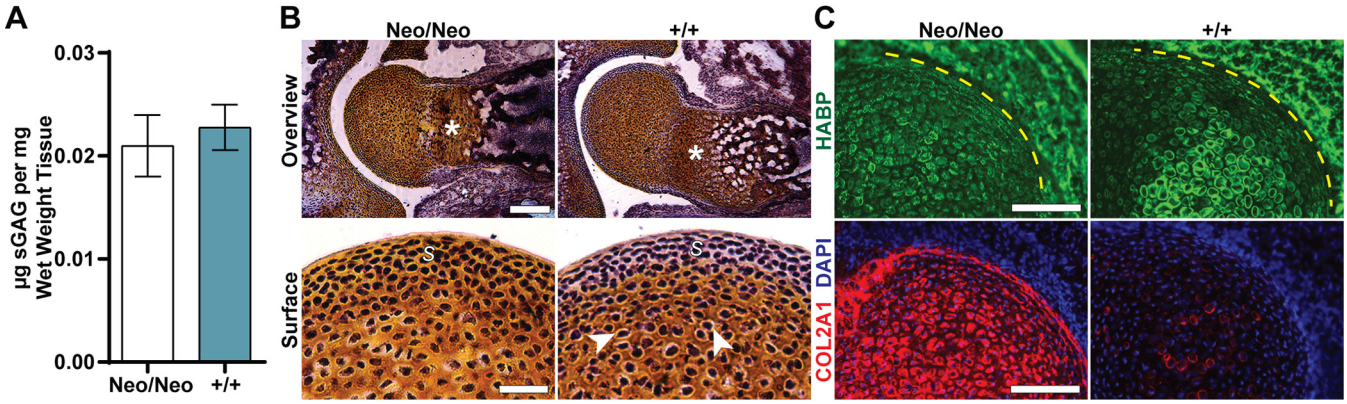

FIG. 2. **Perlecan knockdown affects glycosaminoglycan spatial distribution in P3 articular cartilage.** *A*, A colorimetric assay for sulfated glycosaminoglycans (sGAG) indicated there was no significant difference in sGAG abundance between cartilage isolated from the humerus of Neo/Neo and +/+ P3 mice. Significance was determined using a 2-tailed Student's *t* test. Average of $n = 3$ biological replicates; error bars ± S.D. *B*, Cartilage from the distal humerus of Neo/Neo and +/+ samples stained with safranin O (orange) and hematoxylin (purple) revealed disrupted growth plates (asterisks) and pericellular regions (arrowheads), and an increase in GAG in the articulating surface (*S*) of Neo/Neo samples. Scale bars: Overview: 400 μm, Surface: 100 μm. *C*, Staining for hyaluronic acid (HA) using hyaluronic acid binding protein (HABP; green) indicated a difference in HA expression in the epiphysis of developing cartilage. Articular surface indicated by yellow dashed line. Type II collagen (COL2A1; red) in the distal humeral epiphysis was increased in Neo/Neo samples compared with +/+ littermates. Nuclei were stained with DAPI (blue). Scale bar: 100 μm. Images representative of $n = 3$ biological replicates.

of relative protein abundance as a function of development and perlecan knockdown (42). To summarize LC-MS/MS results, proteins were grouped into tissue compartments (matrisome, cytoskeletal, nuclear, membrane, and other proteins) defined by classifications from the Matrisome and Gene Ontology Projects following (21, 43, 44). We observed an increase in the composition of matrisome and a decrease in nuclear and other proteins between E16.5 and P3 independent of genotype. Although not significantly different, the relative abundance of matrisome was higher in perlecan-deficient mice at P3 than that of +/+ littermates ($p = 0.0868$; Fig. 3*B*). Importantly, HSPG2 knockdown was confirmed (Fig. 3*C*), providing confidence that changes in ECM content can be resolved using our experimental workflow. Volcano plots were generated to facilitate visualization of the global distribution of proteins either as a function of development or perlecan knockdown (supplemental Fig. S3). Changes in protein abundance were more pronounced as a function of development between +/+ E16.5 and P3 timepoints than between Neo/Neo and +/+ cartilage at E16.5 or P3.

To determine the abundance of specific proteins changed as a function of both development and genotype, statistical analyses were performed on individual proteins. Between E16.5 and P3, there was a significant increase in the abundance of 27 matrisome components in +/+ samples, including collagen types II, VI (COL6A1, A2, & A3), IX (COL9A1, A2, & A3), and XI (COL11A1 & A2), biglycan (BGN), cartilage oligomeric matrix protein (COMP), chondroadherin (CHAD), fibronectin (FN1), and matrilin-1 and −3 (MATN1 & 3) (Fig. 3*D*, 3*E*; supplemental Table S1). Significance was determined using a 2-tailed Student's *t* test to analyze individual proteins. Additionally, type XVI collagen (COL16A1), EGF-like repeat and discoidin I-like domain-containing protein 3 (EDIL3), osteomodulin (OMD), sushi repeat-containing proteins (SRPX, SRPX2), and seven other matrisome components were uniquely identified in P3 +/+ cartilage compared with E16.5 +/+ (Fig. 3*F*; supplemental Table S1). Gene Ontology (GO) analysis of all proteins identified in P3 +/+ samples generated fifteen enriched biological process terms including *biomineralization* (GO:0110148) and *response to endogenous stimulus* (GO:0009719, supplemental Fig. S4*A*). Matrix proteins found only in E16.5 +/+ samples when compared with P3 +/+, were collagen triple helix repeat-containing protein 1 (CTHRC1), cathepsin z (CTSZ), galectin-3 (LGALS3), and versican core protein (VCAN) (Fig. 3*F*; supplemental Table S1). Chondroitin sulfate proteoglycan 4 (CSPG4), lectin mannose-binding 1 (LMAN1), serpin H1 (SERPINH1), matrilin-4 (MATN4), and lysyl hydroxylase 3 (PLOD3) were significantly more abundant in E16.5 +/+ cartilage (Fig. 3*D*, 3*E*; supplemental Table S1). GO analysis of E16.5 +/+ proteins generated six enriched biological process terms including *collagen biosynthetic process* (GO:0032964) and *cartilage condensation* (GO:0001502, supplemental Fig. S4*A*).

Perlecan knockdown affected the relative abundance of matrisome components. Epiphycan (EPYC), lumican (LUM), and NID2 were significantly higher in +/+ cartilage, consistent with HSPG2 (Fig. 3*D*, 3*E*; supplemental Table S1). Annexin A6 (ANXA6), CSPG4, and nidogen-1 (NID1) also trended similarly. Within E16.5 samples, only HSPG2 and NID2 were significantly higher in +/+ compared with Neo/Neo littermates. Trypsin 10 (TRY10) abundance was significantly higher in Neo/Neo than Neo/+ cartilage and not present in E16.5 +/+ samples (supplemental Table S1). Prolyl 3-hydroxylase 2 (LEPREL1) was the only matrisome component uniquely identified in E16.5 Neo/Neo cartilage

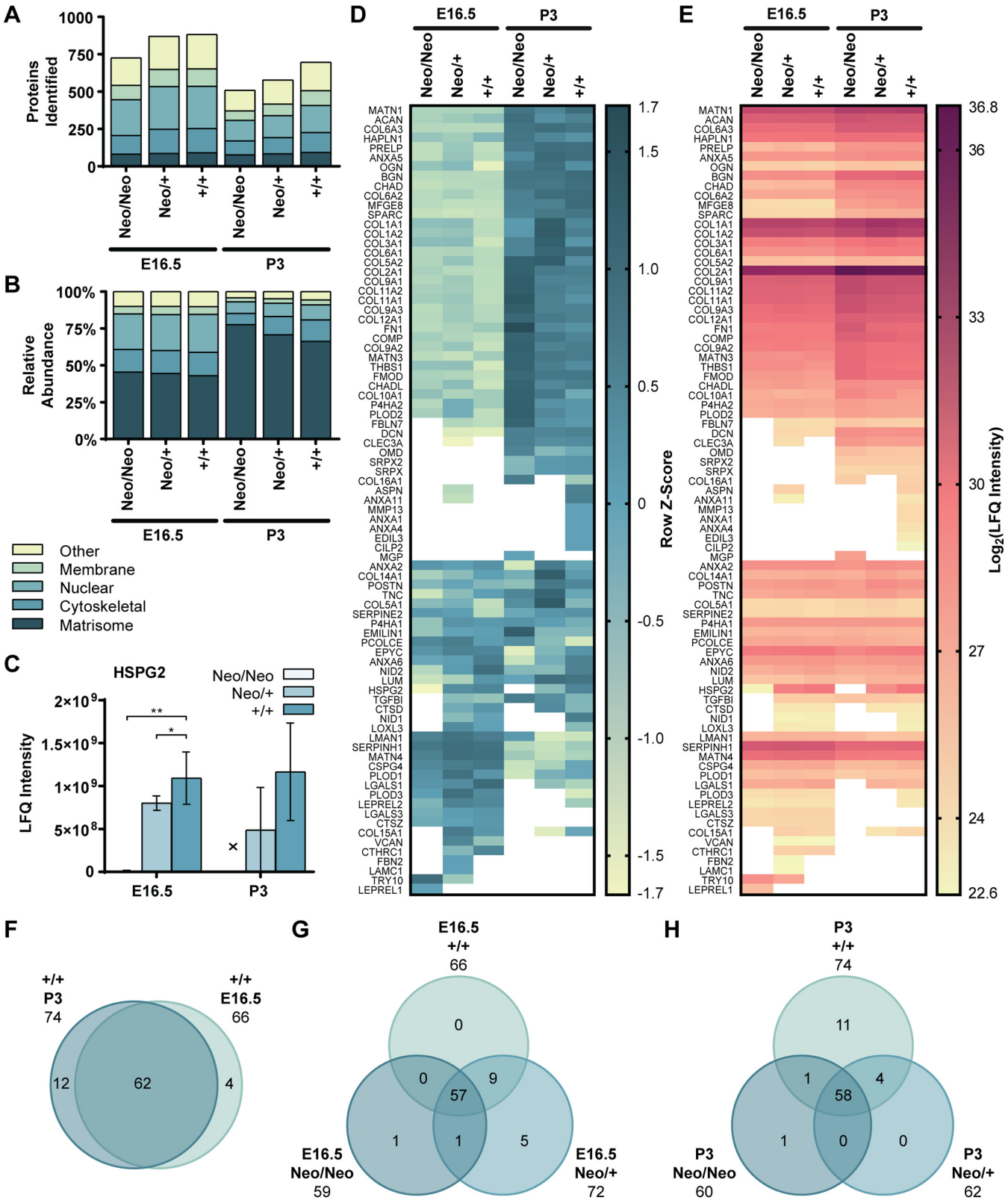

FIG. 3. **Overview of the matrisome of developing murine cartilage.** *A*, Protein identification counts and (*B*) relative abundance of matrisome, cytoskeletal, nuclear, and membrane tissue compartments of the distal humerus as defined by the Matrisome and Gene Ontology Projects (21, 43, 44). *C*, The relative abundance of perlecan (HSPG2) decreased in Neo/+ and Neo/Neo cartilage. One-way ANOVA with post-hoc Tukey-adjusted comparison revealed a significant effect of genotype (* $p < 0.05$, ** $p < 0.01$) at E16.5. Error bars ± S.D. Ð: protein

(Fig. 3*G*). *Proteoglycan metabolic process* (GO:0006029), *regulation of cell adhesion* (GO:0030155), and three other biological process terms were enriched in E16.5 +/+ samples, whereas E16.5 Neo/Neo samples uniquely identified *response to endogenous stimulus* (GO:0009719), *response to transforming growth factor beta* (GO:0071559), and nine additional terms (supplemental Fig. S4*B*).

In contrast to E16.5, perlecan deficiency led to more unique protein identifications and significant differences in protein abundance at P3. At P3, eleven ECM proteins were only observed in +/+ cartilage, including asporin (ASPN), prolyl 3-hydroxylase 3 (LEPREL2), lysyl oxidase homolog 3 (LOXL3), PLOD3, and collagenase 3 (MMP13) (Fig. 3*H*; supplemental Table S1). P3 +/+ cartilage had significantly more EPYC (Fig. 3*D*, 3*E*; (supplemental Table S1). Interestingly, a group of proteins was more abundant in P3 Neo/+ cartilage compared with the other genotypes. Annexin A2 (ANXA2), COL6A1, and LUM were significantly more abundant compared with Neo/Neo samples, and type V collagen (COL5A1 & A2) was significantly more abundant compared with +/+ samples (supplemental Table S1). Collagen types I (COL1A1 & A2), III (COL3A1), and XIV (COL14A1), periostin (POSTN), and tenascin-C (TNC), as well as five other proteins, were also highest in P3 Neo/+ cartilage. Because type I collagen is not typically described as being prevalent in hyaline cartilage, we immunostained for type I collagen and found strong expression on the articulating surface and positive staining within the epiphysis supplemental Fig. S5), consistent with a previous study that reported type I collagen synthesis in developing avian cartilage (45).

Interestingly, many matrisome components were more abundant in the perlecan-deficient cartilage compared with +/+ littermates. P3 Neo/Neo cartilage had significantly more COL9A1 & A2, COL11A1 & A2, COMP, fibromodulin (FMOD), FN1, LMAN1, MATN3, lysyl hydroxylase 2 (PLOD2), and thrombospondin-1 (THBS1). COL2A1, COL10A1, fibulin-7 (FBLN7), procollagen C-endopeptidase enhancer 1 (PCOLCE), and thirteen additional proteins were also more abundant in Neo/Neo cartilage (Fig. 3*D*, 3*E*; supplemental Table S1). GO analysis indicated *collagen biosynthetic process* (GO:0032964) was an enriched term in P3 Neo/Neo samples, whereas *regulation of cell adhesion* (GO:0030155) and *replacement ossification* (GO:0036075) were enriched in P3 +/+ samples (supplemental Fig. S4*C*).

Hydroxyproline and Hydroxylysine Modifications Were Not Affected by Perlecan Knockdown—LC-MS/MS analysis indicated that the abundance of collagen and other matrisome components increased in P3 perlecan-deficient mice; however, this may be because of differences in the solubility of ECM in GuHCl as a function of genotype (Figs. 3, 4*A*). To validate our observation, we used a colorimetric assay to quantify hydroxyproline (Hyp) as a separate way to measure relative collagen abundance (46). Like the LC-MS/MS results, there was a significant increase in Hyp abundance with both age and perlecan knockdown (Fig. 4*B*).

In addition to collagen abundance, we considered the effect of perlecan knockdown on collagen fibril stability. Proline and

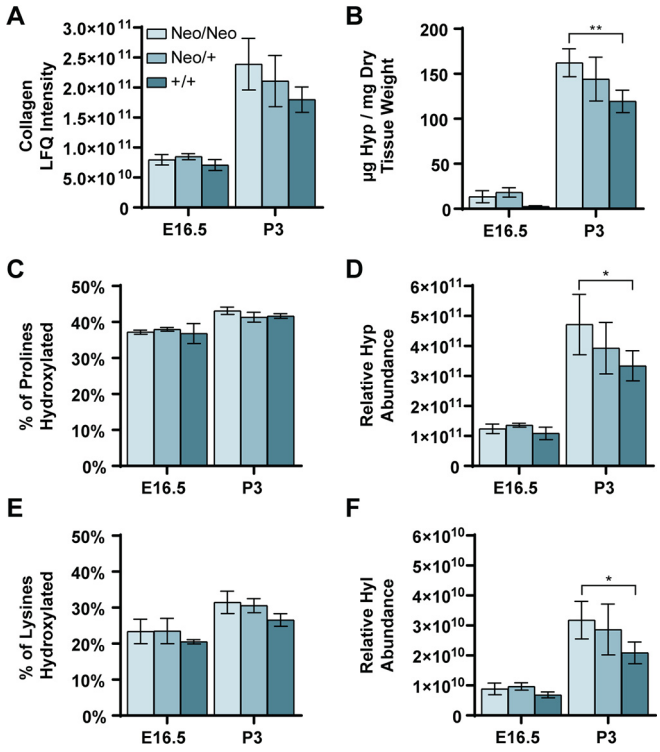

FIG. 4. **Post-translational hydroxylation of collagens is not affected by perlecan knockdown.** *A*, LFQ intensity of collagen peptides increased as a function of age and knockdown at P3. *B*, Hydroxyproline (Hyp) abundance measured using a colorimetric assay was consistent with LC-MS/MS results and revealed a significant increase in Hyp with perlecan knockdown at P3. *C*, Perlecan knockdown did not affect the percentage of prolines hydroxylated. Percentage calculated from LFQ intensity. *D*, The relative abundance of Hyp derived from LFQ intensity of all modified peptides significantly increased in perlecan-deficient P3 mice. *E*, Perlecan knockdown did not affect the percentage of lysines hydroxylated. *F*, Similar to Hyp, the relative abundance of hydroxylysine (Hyl) significantly increased with perlecan knockdown at P3. (*A–F*) The effect of age was significant for all comparisons ($p < 0.0001$). Significance determined by two-way ANOVA and Tukey-adjusted simple effects comparison ($p \geq 0.05$, * $p < 0.05$, ** $p < 0.01$). Results are the average of $n = 3$ biological replicates. Error bars ± S.D.

not identified. (*D*, *E*) Heat maps comparing cross-sample z-scores (*D*) and relative protein abundance (*E*) for the 83 matrisome proteins found in this study. Heat map for z-scores was sorted using biased clustering. White space indicates that protein was not identified. A protein was included if observed in at least 2 of $n = 3$ biological replicates. *F–H*, Venn diagrams indicating the number of matrisome identified as a function of development (*F*) and as a function of perlecan knockdown at E16.5 (*G*) and P3 (*H*). Protein specific results, MaxQuant parameters, and analysis available in supplemental Table S1.

lysine hydroxylation affect triple helix stability and fibril cross-linking, respectively (47, 48). Our LC-MS/MS results indicated prolyl hydroxylases, the enzymes that hydroxylate prolines in the endoplasmic reticulum, were dysregulated; at P3, LEPREL2 was only identified in +/+ samples, whereas P4HA2 abundance increased with perlecan knockdown (Fig. 3*D*, 3*E*; (supplemental Table S1). Furthermore, PLODs, which hydroxylate lysine in the endoplasmic reticulum, were also differentially regulated by perlecan knockdown. PLOD2 abundance significantly increased whereas PLOD1 decreased, and PLOD3 was not identified in P3 perlecan-deficient mice (Fig. 3*D*, 3*E*; (supplemental Table S1).

To investigate the degree of proline and lysine hydroxylation, we included Hyp and hydroxylysine (Hyl) as variable modifications when the LC-MS/MS spectra were analyzed using MaxQuant. The percent of prolines hydroxylated was unchanged with perlecan knockdown (Fig. 4*C*), and the relative abundance of peptides with Hyp modifications mimicked the collagen trends (Fig. 4*A*, 4*D*). Similarly, perlecan knockdown did not significantly affect the level of lysine hydroxylation (Fig. 4*E*). The relative abundance of proteins with Hyl modifications had a trend analogous to total collagen and Hyp, increasing from E16.5 to P3, as well as with knockdown at P3 (Fig. 4*A*, 4*D*, 4*F*).

Perlecan Knockdown Did Not Affect Collagen Fibril Diameter or Area Fraction in Developing Cartilage—The addition of perlecan to *in vitro* culture increased the diameter of type I and type II collagen fibrils (49); therefore, we hypothesized that the increase in collagen abundance observed in P3 Neo/Neo mice was because of an increase in density of smaller diameter fibrils. TEM of distal humeral cartilage revealed dark fibrils with the periodic banding structure of the fibril-forming collagens (supplemental Fig. S6), which were randomly distributed in Neo/Neo and +/+ cartilage (Fig. 5*A*, *B*). These fibrils were presumed to be made up of primarily type II collagen and accessory molecules known to mediate fibril diameter (*e.g.* collagens IX and XI) (50). Fibrils in the center of the epiphysis appeared to be less organized than at the surface of the cartilage but were similar between Neo/Neo and +/+ littermates (Fig. 5*C*–5*F*). There was no significant difference in fibril area fraction between genotypes or cartilage regions (Fig. 5*G*). Although the average diameter of fibrils in the center of the epiphysis was smaller than of those near the articulating surface for +/+ cartilage, it was not significantly smaller in perlecan-deficient mice (Fig. 5*H*).

Perlecan Knockdown Leads to Increased Protein Secretion Ex Vivo—Unable to visualize a major difference in bulk matrix ultrastructure, we hypothesized that the excess matrisome observed in P3 Neo/Neo cartilage was secreted into the interstitial space but not integrated into the overall ECM network. To quantify protein secretion, we incubated freshly harvested P3 distal humeri *ex vivo* for 4 days and collected and replaced the media every 2 days, an incubation period known to maintain chondrocyte viability (51, 52). Notably,

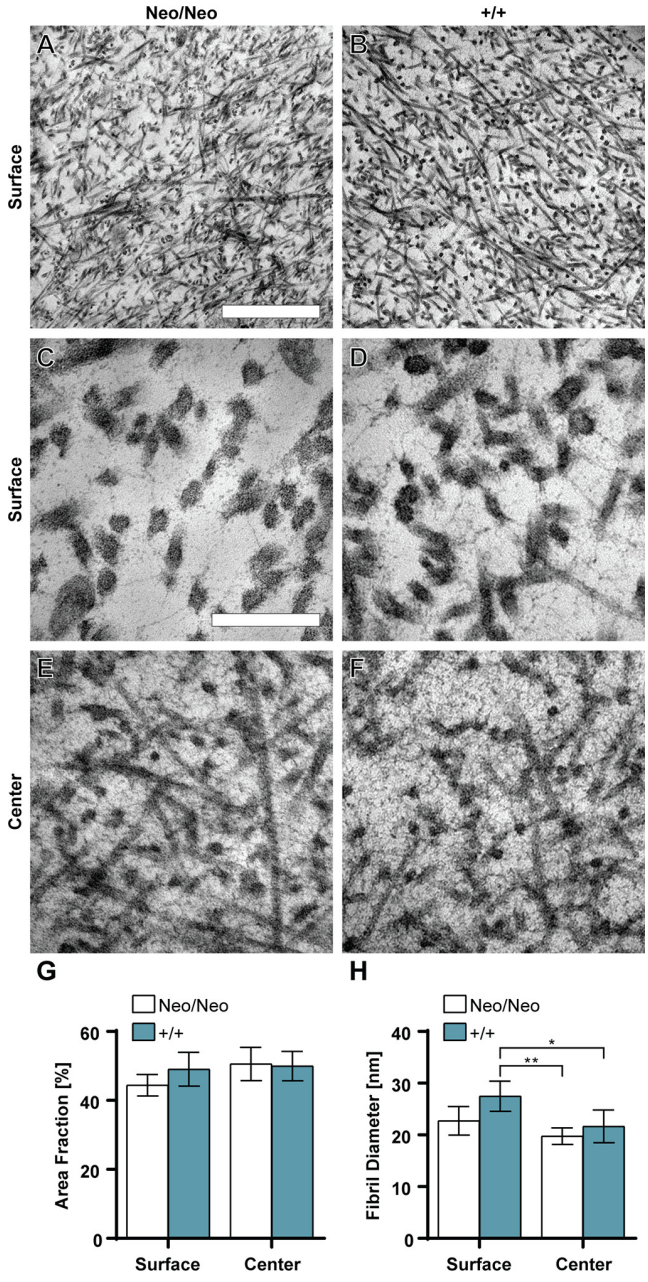

FIG. 5. **Perlecan knockdown does not substantially affect epiphyseal fiber architecture.** Representative TEM images of P3 cartilage from Neo/Neo mice (*A*, *C*, *E*) and +/+ littermates (*B*, *D*, *F*) at 30,000× (*A*, *B*) and 120,000× (*C*, *D*, *E*, *F*). Regions were selected near the articulating surface (Surface, *A*–*D*) or within the center of the epiphysis (Center, *E*, *F*) of the distal humerus. Scale bars: 750 nm and 200 nm, for (*A*, *B*) and (*C*, *D*, *E*, *F*), respectively. (*G*) Perlecan knockdown did not affect fibril area fraction within the interstitial matrix. Results were averaged over three different images for $n = 4$ biological replicates. (*H*) Similarly, perlecan knockdown did not significantly affect fibril diameter; however, interstitial matrix within the center of the epiphysis had significantly smaller fibril diameters than near the surface ($p = 0.0066$). Significance determined by two-way ANOVA and post-hoc Tukey-adjusted comparison (* $p < 0.05$, ** $p < 0.01$). Results averaged over ≥ 27 randomly chosen, transversely oriented fibrils for $n = 4$ biological replicates. Error bars ± S.D.

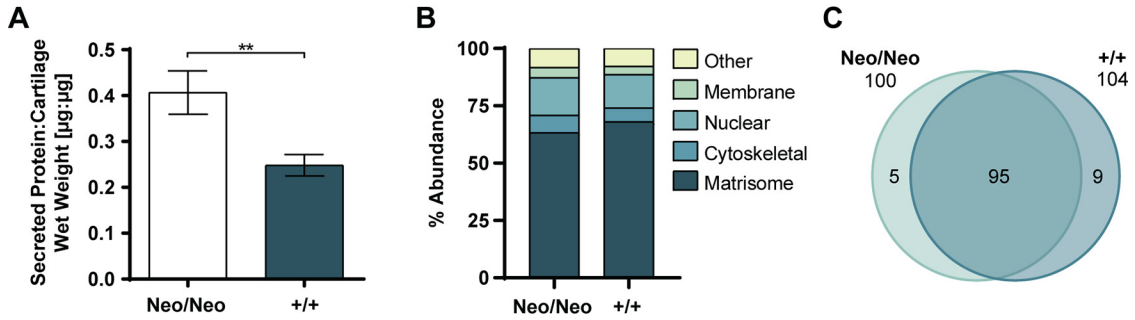

FIG. 6. **Perlecan knockdown affects cartilage secretome.** *A*, Significantly more protein was secreted by P3 Neo/Neo cartilage explants as determined by normalizing the amount of protein in the supernatant by that in the explant. Results are reported as an average of $n = 3$ or 4 biological replicates. Significance was determined using a 2-tailed Student's *t* test (** $p < 0.01$). Error bars ± S.D. *B*, There were no significant differences in the compartments of proteins secreted by either genotype. *C*, Venn diagram of matrisome identified in Neo/Neo and +/+ secretomes. Protein specific results, MaxQuant parameters, and analysis available in supplemental Table S2.

cartilage is suitable for *ex vivo* incubation studies because of its relatively avascular and aneural composition (53). During the incubation period, significantly more protein was secreted by Neo/Neo compared with +/+ cartilage explants ($p = 0.0033$; Fig. 6*A*). All proteins identified in the supernatant are referred to as the "secretome."

There were no significant differences in the relative abundance of different tissue compartments between genotypes ($p > 0.9999$; Fig. 6*B*). Volcano plots were generated to visualize dysregulated proteins as a function perlecan knockdown (supplemental Fig. S7). Of the 109 matrisome components found, five were uniquely identified in Neo/Neo samples, including COL10A1 (Fig. 6*C*; supplemental Table S2). Conversely, type XVIII collagen (COL18A1), cathepsin B (CTSB), cathepsin L1 (CTSL), matrilin-2 (MATN2), matrix metalloproteinase-3 (MMP3), and four additional proteins were unique to +/+ samples (Fig. 6*C*; supplemental Table S2). HSPG2, BGN, collagen type XV (COL15A1), MATN1, and lactadherin (MFGE8) were significantly less abundant in the secretome of Neo/Neo mice as determined using a 2-tailed Student's *t* test on individual proteins, whereas COL2A1 and NID2 were significantly more abundant in Neo/Neo mice (supplemental Fig. S7; supplemental Table S2). Interestingly, alpha-2-macroglobulin-P (A2MP), a proteinase inhibitor (54), was also increased in perlecan-deficient mice. COL11A1, LOXL3, MATN4, NID1, metalloproteinase inhibitor 1 (TIMP1), and TNC were also less abundant in the Neo/Neo secretome (supplemental Fig. S7; supplemental Table S2).

Chondrocyte Volume Increases in Perlecan-deficient Cartilage—Increased protein secretion in Neo/Neo explants may account for the abundant matrisome observed in cartilage LC-MS/MS results; however, the difference in matrisome composition may also be explained by an increased ECM to cell volume fraction in perlecan-deficient cartilage. To accurately measure how perlecan knockdown affected chondrocyte size and matrix volume fraction, we generated three-dimensional geometries based on the native physiology. Decellularized humeri from P3 Neo/Neo and +/+ mice were stained with wheat germ agglutinin (WGA), which labels a subset of proteoglycans in the remaining ECM. Confocal images acquired near the articulating surface of the distal humerus were processed in MATLAB to generate cellular and ECM geometries following (18) (Fig. 7*A*, 7*B*). The average volume of individual cells in perlecan-deficient cartilage was significantly higher than in +/+ littermates ($V_{Neo/Neo} = 326.02\ \mu m^3 \pm 27.53$, $V_{+/+} = 183.16\ \mu m^3 \pm 82.56$, average ± S.D., $p = 0.0467$, Fig. 7*C*). Nevertheless, cellular volume fraction (ϕ) calculated from the geometries trended toward less ECM in the Neo/Neo samples, but were not significantly different between Neo/Neo and +/+ samples ($\phi_{Neo/Neo} = 18.65\% \pm 0.75\%$, $\phi_{+/+} = 16.46\% \pm 1.30\%$, average ± S.D., $p = 0.0642$, Fig. 7*D*).

We previously demonstrated that age-related changes in cell-ECM geometry affected the strain experienced by the ECM when cartilage was modeled *in silico* (18). To test if changes in chondrocyte volume because of perlecan knockdown affected the distribution of strain, we combined the physiologically relevant geometries generated from confocal imaging with experimentally determined compressive moduli we previously measured using AFM (supplemental Table S3) (15). The geometries were deformed by 5% unconfined compression using ANSYS (Fig. 7*E*), which is within the expected physiological range of 1–10% (55, 56). Simulations were run where the geometry and material properties matched the genotype, and then were mismatched, to see how both affected the resultant strain. ECM strain in Neo/Neo cartilage was significantly decreased compared with +/+ samples (Fig. 7*F*). Interestingly, chondrocytes experienced similar strains in response to applied compression even though the compressive moduli and individual cell volumes were significantly different as a function of perlecan knockdown (Fig. 7*G*).

DISCUSSION

The limited understanding regarding how cartilage forms during development hinders the design of early intervention methods to treat or prevent damaged cartilage. Additionally, the development of therapies for SJS and other cartilage diseases are inhibited by a lack of understanding of how

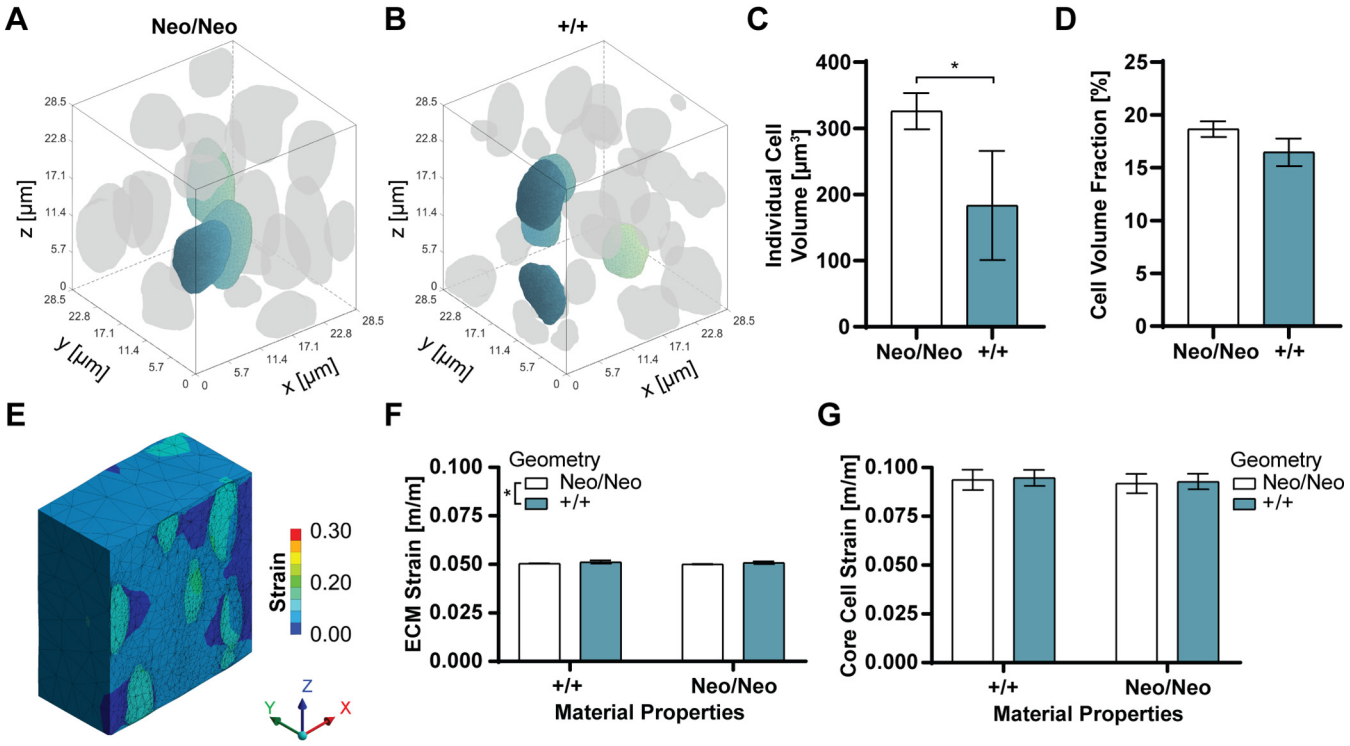

FIG. 7. **Individual chondrocyte volume significantly increased because of perlecan knockdown.** Representative cellular geometries from P3 Neo/Neo (*A*) and +/+ (*B*) humeri. Origin indicates the 3–4 cell layers within the articulating surface ($x = 0$). Cells within 1 μm of the boundary were not used for volume or strain calculations because of incomplete geometries and boundary edge effects. *C*, The volume of individual chondrocytes from Neo/Neo mice were 78.0% larger than those from +/+ littermates. *D*, The volume fraction occupied by cells was not significantly different as a function of genotype. *E*, Finite element models based on the geometries were compressed 5% in the *x*-direction using ANSYS and revealed a slight, but significant decrease in ECM strain with the perlecan knockdown (*F*) whereas there was no difference in the strain experienced by the chondrocytes (*G*). ECM strain was (from left to right) 0.0504 ± 0.0001, 0.0512 ± 0.0008, 0.0500 ± 0.0002, 0.0508 ± 0.0007 (*F*). Core cell strain was (from left to right) 0.0937 ± 0.0052, 0.0946 ± 0.0041, 0.0917 ± 0.0050, 0.0927 ± 0.0040 (*G*) (Mean ± S.D.). Three different areas from the articular surface were imaged and results were averaged over $n = 3$ biological replicates. Significance was determined using a 2-tailed Student's *t* test (*C*, *D*) or two-way ANOVA (*F*, *G*) (* $p < 0.05$). Error bars ± S.D.

perlecan deficiency affects the functionality of cartilage and leads to osteoarthritis. Although perlecan has been implicated in chondrogenic differentiation (3), cell-matrix mechanotransduction (2, 4), and chondrocyte mechanical protection (1), the effect of perlecan deficiency on the overall organization and composition of the matrisome of developing cartilage has not been explored. Resolving these effects will provide more insight into the role of perlecan on healthy cartilage development, as well as the progression of SJS and other chondrodysplasias.

Murine Cartilage Matrisome Significantly Changes During Development—Proteomic analysis of developing cartilage revealed significant changes in protein expression during ECM remodeling within the epiphyses of E16.5 and P3 +/+ mice (Fig. 3, supplemental Table S1). Consistent with previous findings, matrisome components identified in E16.5 and P3 cartilage were categorized primarily as *collagen-containing extracellular matrix* (GO:0062023) (57). Of the 78 matrisome identified in +/+ samples, 48 were differentially expressed or uniquely identified between timepoints. ECM identified at E16.5 reflected components known to be found during early matrix biosynthesis and organization (*e.g.* LGALS3 and SERPINH1) (58, 59). These observations are supported by the enrichment of the GO biological process terms *collagen biosynthetic process* (GO:0032964) and *cartilage condensation* (GO:0001502, supplemental Fig. S4*A*). In contrast, the P3 matrisome was enriched in proteins related to ECM maturation and collagen fibril accessory proteins including COL9A3, COL11A1 & 2, and decorin (DCN) (60, 61). Chondrocyte differentiation markers, COMP and CHAD, also emerged at P3, which correlate with chondrocyte maturation and progression toward ossification (62, 63). In addition to enrichment of *biomineralization* (GO:0110148) and *response to endogenous stimulus* (GO:0009719) biological process terms, more proteins that are included in the shared terms (*e.g. collagen fibril organization* GO:0030199, *extracellular matrix organization* GO:0030198) are up-regulated or unique to P3 +/+ compared with E16.5 +/+ samples (supplemental Fig. S4*A*).

Perlecan Knockdown Decreases Abundance of PCM Proteins—Comparison of matrisome expression between cartilage from perlecan-deficient and healthy littermates revealed many differences in ECM composition. We observed reduced

NID2 immunofluorescence in the PCM and smaller pericellular regions stained with safranin O in perlecan-deficient P3 cartilage (Figs. 1*B*, 2*B*). Furthermore, LC-MS/MS indicated NID2, NID1, and COL15A1 were less abundant because of perlecan knockdown (Fig. 3*D*, 3*E*). These proteins are binding partners of perlecan, share similar protein domains, and colocalize in the PCM (5, 38). Analysis of the secretome of cartilage explants revealed decreased secretion of NID1 and COL15A1 with the knockdown, whereas NID2 was increased (supplemental Table S2). The absence of perlecan as a binding partner, combined with the known compensatory expression of nidogens (64, 65), may explain the excess NID2 secreted by Neo/Neo cartilage *in vitro*. We postulate that perlecan knockdown leads to the reduction of NID1 synthesis, resulting in an increase in NID2 synthesis. Because there is minimal perlecan in Neo/Neo cartilage, NID2 was not strongly bound to the PCM and released into the media. NID1, NID2, and COL15A1 were also significantly less abundant in the proteome of the residual cartilage after *ex vivo* incubation (supplemental Table S2), indicating that NID2 is not able to incorporate into the PCM. Notably, *regulation of cell adhesion* (GO:0030155) and *proteoglycan metabolic process* (GO:0006029) biological process terms were enriched in +/+ samples (supplemental Fig. S4). These results support previous observations that perlecan knockdown disrupted PCM formation during cartilage development (8). PCM composition and mechanics have been reported to play critical roles in protecting chondrocytes from mechanical loading (1, 2), and disruption may lead to changes in bulk matrix composition and integrity, contributing to the disease progression observed in SJS patients.

Perlecan Regulates Endochondral Ossification During Cartilage Development—COL10A1 immunostaining was increased in Neo/Neo epiphyses (Fig. 1*C*). Previous reports that investigated perlecan null mice indicated no change in type X collagen expression in E15.5 and E18.5 cartilage (10, 20), whereas we found little difference in abundance at E16.5. Innate differences in between the perlecan-deficient and null models may account for this inconsistency, as well as our observation that there was no significant change in the matrix ultrastructure of perlecan-deficient mice, whereas the collagen network was disrupted in perlecan null mice (10). Our LC-MS/MS results also revealed that COL10A1 and OMD were increased in abundance in perlecan-deficient cartilage by P3 (Fig. 3*D*, 3*E*). Hypertrophic chondrocytes express COL10A1 during endochondral ossification (19), and OMD is known to suppress cartilage matrix formation prior to ossification (66). In addition, chondrocyte volume increased because of perlecan knockdown (Fig. 7*C*), and COL10A1 was only secreted by Neo/Neo samples (supplemental Table S2). Conversely, the secretome of +/+ cartilage uniquely contained matrix gla protein (MGP, supplemental Table S2) known to inhibit cartilage ossification (67). The differences in these markers supports the observation that ectopic ossification occurs in Neo/Neo cartilage (22) and likely leads to the premature growth plate closure and shortened long bones observed in SJS patients (6). Alternatively, enrichment for *response to endogenous stimulus* (GO:0009719) and *response to transforming growth factor beta* (GO:0071559) terms in E15.6 Neo/Neo and P3 +/+ samples suggests that ossification and chondrocyte hypertrophy is beginning earlier in perlecan-deficient cartilage (supplemental Fig. S4).

Matrisome Compensation in Perlecan-deficient Cartilage—Although we hypothesized that perlecan knockdown would decrease the abundance of PCM proteins, we did not expect to find an increase in bulk matrisome components (*e.g.* COL2A1, COMP, and FN1) (Fig. 3*D*, 3*E*). Protein solubility is a major factor that influences the proteomic analysis of ECM-rich tissues and some enzymes associated with collagen crosslinking were dysregulated because of perlecan knockdown (*e.g.* PLOD1, 2, & 3, LEPREL2; Fig. 3*D*, 3*E*). However, the greater matrisome abundance did not appear to be caused by an increase in extractability. Overall Hyp abundance, measured using an assay with stronger extraction conditions than for LC-MS/MS, was also increased in perlecan knockdown cartilage, indicating the increase in bulk matrix in Neo/Neo mice was not an artifact of differences in solubility (Fig. 4*A*). Hyp and Hyl modification levels, indicative of collagen triple helix stability and fibril crosslinking, were not affected by perlecan knockdown (Fig. 5*C*, 5*E*). Additionally, immunofluorescent staining revealed an increase in type II collagen in Neo/Neo cartilage, consistent with the proteome and secretome results (Figs. 2*C*, 3*D*, 3*E*; supplemental Table S1).

It is counterintuitive that perlecan deficiency will lead to an increase in type II collagen and other bulk matrisome abundance, although elevated mRNA levels of COL2A1, MATN3, and COMP were previously reported in perlecan-null embryos (10). Interestingly, *collagen biosynthetic process* (GO:0032964) is enriched in P3 Neo/Neo samples (supplemental Fig. S4C). Additionally, the proteins up-regulated in Neo/Neo samples that intersect the top five shared P3 terms are bulk matrix proteins (*e.g.* COL11A1, MATN3, and COMP). The spatio-temporal localization of perlecan during healthy development may provide an explanation for the increased matrisome abundance that emerges with perlecan knockdown. Perlecan is ubiquitously expressed in the cartilage template at E16.5 in WT mice (15). Although there were few differences in the overall matrisome at E16.5, the effects of perlecan deficiency may take time to manifest within the tissue. By P3, perlecan is restricted to the PCM in healthy cartilage, and functional perlecan is not available in the P3 Neo/Neo cartilage to orchestrate the assembly of the bulk matrix. If the chondrocytes sense incorrect matrix assembly, because of the absence of a PCM that is thought to protect from mechanical loading and mediate growth factor signaling (2, 4), bulk matrix synthesis may be increased to counteract the absence of the PCM. However, the developing ECM network in perlecan-deficient cartilage is unable to incorporate the

excess proteins for reasons that currently remain unclear. Interestingly, models that knockout other components of the PCM do not report overproduction of bulk ECM. Type VI collagen-null mice showed no change in perlecan expression in adult articular cartilage (68) and type XXVII collagen-null mice reported no change in type II or X collagen expression in E14.5 epiphyseal cartilage and the growth plate (69).

Excess Matrix Is Not Incorporated Into the ECM Network of Perlecan Knockdown Cartilage—Collagen fibril assembly *in vitro* is accelerated in the presence of chondroitin sulfate enriched perlecan fragments (49), indicating perlecan deficiency would lead to disrupted matrix ultrastructure. In addition, when perlecan was knocked out *in vivo*, collagen fibrils in the growth plate appeared shorter (10); however, we observed no difference in collagen fibril area fraction and fibril diameter between the epiphyses of P3 Neo/Neo and +/+ littermates (Fig. 5). These discrepancies may be attributed differences in model systems and locations within developing cartilage. Additionally, cellular and matrix geometries generated from WGA-stained decellularized cartilage revealed no significant difference in volume fraction as a function of perlecan knockdown (Fig. 7*D*).

Because neither ultrastructure nor matrix volume fraction could account for the increased matrisome abundance in Neo/Neo cartilage, we then tested if the excess ECM was not incorporating into the developing network. Incubation of explants *in vitro* confirmed that more protein was released from perlecan-deficient cartilage, which may explain why there was no significant difference in the fibril diameter or area fraction (Figs. 5, 6*A*). Alternatively, degradation may be affected, leaving excess matrisome to be secreted but not broken down. Proteomic analysis of secreted proteins revealed that CTSB, CTSL, and MMP3 were exclusively identified in the +/+ secretome. Heparan sulfate GAGs bound to perlecan are known to sequester cathepsins and provide the acidic environment necessary to maintain endopeptidase activity (70). These collagen degradation enzymes may fine-tune ECM assembly in +/+ cartilage (71, 72), and reduced enzyme abundance and activity could explain the increase in matrix proteins in Neo/Neo cartilage (Fig. 3*D*, 3*E*). In addition, the proteinase inhibitor A2MP was significantly more abundant in Neo/Neo secretome (54) (supplemental Table S2) and the GO biological process term *replacement ossification* (GO:0036075) was only attributed to P3 +/+ (supplemental Fig. S4*C*), providing further evidence that matrisome turnover is affected by perlecan knockdown.

Although there was no significant difference in the level of post-translational collagen hydroxylation (Fig. 4), crosslinking may be affected by perlecan knockdown. Specifically, lysyl oxidase-like proteins (LOXL2 & 3) were less abundant in the perlecan-deficient secretome (supplemental Table S2), whereas LOXL3 was uniquely identified in P3 +/+ cartilage (supplemental Table S1). Decreased LOXL3, combined with an increase in COL2A1 secretion (supplemental Table S2), indicates that type II collagen trimers secreted by chondrocytes were not stably incorporated into the bulk matrix of perlecan-deficient cartilage.

Haploinsufficiency of Perlecan Alters Developing Cartilage Matrisome—Interestingly, some ECM proteins were elevated in Neo/+ but not Neo/Neo mice. These proteins included COL1A1 & A2, COL3A1, COL5A1 & A2, TNC, and POSTN. The abundance of these collagens is known to increase early in bone fracture callus formation (73, 74), and TNC and POSTN are associated with the fibrotic response to injury (75, 76). Perlecan haploinsufficiency may be interpreted as damaged tissue by chondrocytes, leading to a pseudo-fibrotic response. However, the lack of a further increase of these ECM proteins in Neo/Neo mice suggests that the effect of perlecan is not linearly correlated with the overall concentration. Further work is necessary to confirm that a mild decrease in perlecan abundance evokes a fibrotic response in cartilage.

Perlecan Supports Articular Cartilage Mechanics by Regulating GAG Deposition—It was previously shown that perlecan knockdown leads to decreased GAG abundance in the developing growth plate of long bones (8, 10, 20, 22). In contrast, a recent report showed that GAG deposition was increased in the vertebral growth plates of heparan sulfate-deficient, *Hspg2* exon 3-null mice resulting in accelerated chondrocyte hypertrophy and abnormal bone formation (41). Our study of the developing epiphysis also revealed an increase in GAGs with perlecan knockdown. Although a biochemical assay for sGAGs indicated no significant difference between genotypes, safranin O staining showed an overall increase in GAG deposition near the articulating surface of P3 perlecan-deficient mice, which may be attributed to differential expression of HA (Fig. 2). AFM studies of the bulk matrix in hyaluronidase-treated bovine cartilage (77) and heparinase-treated porcine cartilage (1) showed an increase in compressive modulus when GAG networks were broken down. Interestingly, we previously demonstrated that there was a decrease in compressive moduli of bulk matrix and chondrocytes at the articulating surface of *Hspg2*$^{C1532Y-Neo}$ mice compared with wildtype littermates (15). Together, the AFM, safranin O, and HABP results indicate that perlecan influences GAG deposition in developing articular cartilage, ultimately decreasing the compressive modulus of the bulk matrix.

In addition to altered mechanical properties, we observed an increase in cell size near the articulating surface (Fig. 7*A*, 7*B*). The chondrocytes in Neo/Neo cartilage may be generally larger than those of +/+ littermates, but increased size is also indicative of hypertrophy. Indeed, perlecan-deficient adult mice have a reduced amount of articular cartilage (8). The expansion of the hypertrophic zone, combined with the decreased compressive modulus near the articulating surface of Neo/Neo samples could impact the ability of cartilage to withstand cyclic loading and lead to the early damage and onset of osteoarthritis observed in perlecan-deficient mice and SJS patients (6, 8).

Perlecan Knockdown Affects Chondrocyte Geometry and Mechanics—Although chondrocyte volume was significantly larger in Neo/Neo cartilage (Fig. 7*C*), the similarity in cellular volume fraction compared with +/+ tissue indicated that the increase in matrisome was not because of changes in cell-matrix volumetric distributions. Interestingly, the volume fractions for the P3 +/+ cartilage were the same as in our previous study that used a different strain of mice (18), demonstrating the repeatability of this method for generating physiologically relevant geometries.

In addition to measuring cell volume, the three-dimensional geometries enabled us to simulate compressive loading and examine the biomechanical response of perlecan-deficient and healthy ECM and chondrocytes. The changes in geometry primarily contributed to the decreased strain experienced by the ECM ($p = 0.0412$), and not the change in material properties ($p = 0.2801$) as determined by two-way ANOVA (Fig. 7*G*). Notably, cellular strain was not different between Neo/Neo and +/+ tissues, and neither geometry ($p = 0.7146$) nor material properties ($p = 0.4902$) significantly contributed (Fig. 7*F*). This may indicate the chondrocytes are adapting to the lack of perlecan by reorganizing the ECM to maintain constant average strain within the cells. Cellular strain was amplified ~1.84-fold compared with ECM strain, like previous reports (18, 78–80). Overall, these results suggest that chondrocytes increase their size and adjust their metabolism in the absence of perlecan to maintain constant strain.

In summary, we report the how the proteomic composition of developing murine cartilage significantly changes as a function of development and perlecan knockdown. Our analysis provides additional support that perlecan plays important roles in the formation of a functional PCM, restriction of GAGs from articular cartilage, and inhibition of endochondral ossification. Furthermore, the increase in GAGs may explain why we previously observed that the compressive modulus of articular cartilage decreases in perlecan-deficient mice (15). These results suggest that chondrocytes are compensating for the lack of perlecan by secreting excess ECM to counteract decreased matrix integrity; however, it is not able to incorporate into the network. SJS disease progression and the events that lead to the osteoarthritic phenotype are becoming more evident, but the underlying mechanisms by which perlecan delays hypertrophy in articular cartilage remains unclear. Future studies that directly quantify matrix crosslinking, such as biochemical assays or reverse-phase high-performance liquid-chromatography, may better elucidate the effect of perlecan knockdown on fibrillar matrix integrity and ultimately the functionality of cartilage.

DATA AVAILABILITY

The mass spectrometry proteomics data have been deposited in the MassIVE repository under the DOIs, MassIVE accession numbers: 10.25345/C5BT0W, MSV000084324 (Cartilage) and 10.25345/C5Z66J, MSV000084384 (Secretome) [29,33].

Acknowledgments—We thank Victoria Hedrick for her consultation and LC-MS/MS operation at the Purdue Proteomics Core. Additionally, the authors acknowledge Wenbin Zhu at the Purdue Statistical Consulting Service and Robert Seiler at the Purdue Life Science Microscopy Facility for their contributions and consultation.

Funding and additional information—Declaration of Funding: This work was supported by the National Institutes of Health [R01 AR071359 to S.C and T.L.K. and DP2 AT009833 to S.C.] and the Charles C. Chappelle Fellowship [to A.R.O.].

Author contributions—A.R.O., T.L.K.-U., and S.C. designed research; A.R.O., M.M.K., and S.C. performed research; A.R.O., M.M.K., and S.C. analyzed data; A.R.O., M.M.K., and S.C. wrote the paper.

Conflict of interest—Authors declare no competing interests.

Abbreviations—The abbreviations used are: ECM, extracellular matrix; SJS, schwartz-jampel syndrome; LC-MS/MS, liquid chromatography–tandem mass spectrometry; PCM, pericellular matrix; ERK, extracellular signal-regulated kinase; GAG, glycosaminoglycan; sGAG, sulfated glycosaminoglycan; Neo/+, heterozygous *Hspg2*$^{C1532Y-Neo}$; Neo/Neo, homozygous *Hspg2*$^{C1532Y-Neo}$; +/+, wildtype; E16.5, embryonic day 16.5; P3, postnatal day 3; TEM, transmission electron microscopy; OCT, optimal cutting temperature; RT, room temperature; PFA, paraformaldehyde; MOM, mouse on mouse; COL10A1, type X collagen; NID*x,* nidogen-*x*; HSPG2, perlecan protein; *Hspg2,* perlecan gene; COL2A1, type II collagen; DAPI, 4′,6-diamidino-2-phenylindole; DMB, dimethylmethylene blue; Hyp, hydroxyproline; Hyl, hydroxylysine; ROI, region of interest; WGA, wheat germ agglutinin; AFM, atomic force microscopy; FDR, false discovery rate; HA, hyaluronic acid; HABP, hyaluronic binding protein; LFQ, label-free quantification; COL6A*x,* type VI collagen alpha-*x*; COL9A*x,* type IX collagen alpha-*x;* COL11A*x,* type XI collagen alpha-*x;* BGN, biglycan; COMP, cartilage oligomeric matrix protein; CHAD, chondroadherin; FN1, fibronectin; MATN*x,* matrilin-*x*; OMD, osteomodulin; LGALS3, galectin-3; CSPG4, chondroitin sulfate proteoglycan 4; LMAN1, lectin mannose-binding 1; SERPINH1, serpin H1; PLOD*x,* lysyl hydroxylase *x*; EPYC, epiphycan; LUM, lumican; LEPREL2, Prolyl 3-hydroxylase 3; LOXL*x,* lysyl oxidase homolog *x*; COL5A*x,* type V collagen alpha-*x*; COL1A*x,* type I collagen alpha-*x*; COL3A1, type III collagen; POSTN, periostin; TNC, tenascin-C; CTSB, cathepsin B; CTSL, cathepsin L1; MMP3, Matrix metalloproptinase-3; COL15A1, type XV collagen; A2MP, alpha-2-macroglobulin-P.

Received February 21, 2020, and in revised form, May 5, 2020
Published, MCP Papers in Press, May 7, 2020, DOI 10.1074/mcp.RA120.001998

REFERENCES

1. Wilusz, R. E., DeFrate, L. E., and Guilak, F. (2012) A biomechanical role for perlecan in the pericellular matrix of articular cartilage. *Matrix Biol.* **31,** 320–327
2. Guilak, F., Alexopoulos, L. G., Upton, M. L., Youn, I., Choi, J. B., Cao, L., Setton, L. A., and Haider, M. A. (2006) The pericellular matrix as a transducer of biomechanical and biochemical signals in articular cartilage. *Ann. N.Y. Acad. Sci.* **1068,** 498–512
3. French, M. M., Smith, S. E., Akanbi, K., Sanford, T., Hecht, J., Farach-Carson, M. C., and Carson, D. D. (1999) Expression of the heparan sulfate proteoglycan, perlecan, during mouse embryogenesis and perlecan chondrogenic activity in vitro. *J. Cell Biol.* **145,** 1103–1115
4. Vincent, T.L., McLean, C.J., Full, L.E., Peston, D., and Saklatvala, J. (2007) FGF-2 is bound to perlecan in the pericellular matrix of articular cartilage, where it acts as a chondrocyte mechanotransducer. *Osteoarthr. Cartil.* **15,** 752–763
5. Farach-Carson, M. C., Warren, C. R., Harrington, D. A., Carson, D. D. (2014) Border patrol: Insights into the unique role of perlecan/heparan sulfate proteoglycan 2 at cell and tissue borders. *Matrix Biol.* **34,** 64–79
6. Arikawa-Hirasawa, E., Wilcox, W. R., Le, A. H., Silverman, N., Govindraj, P., Hassell, J. R., and Yamada, Y. (2001) Dyssegmental dysplasia, Silverman-Handmaker type, is caused by functional null mutations of the perlecan gene. *Nat. Genet.* **27,** 431–434
7. Nicole, S., Davoine, C. S., Topaloglu, H., Cattolico, L., Barral, D., Beighton, P., Hamida, D. B., Hammouda, H., Cruaud, C., White, P. S., Samson, D., Urtizberea, J. A., Lehmann-Horn, F., Weissenbach, J., Hentati, F., and Fontaine, B. (2000) Perlecan, the major proteoglycan of basement membranes, is altered in patients with Schwartz-Jampel syndrome (chondrodystrophic myotonia). *Nat. Genet.* **26,** 480
8. Rodgers, K. D., Sasaki, T., Aszodi, A., and Jacenko, O. (2007) Reduced perlecan in mice results in chondrodysplasia resembling Schwartz–Jampel syndrome. *Hum. Mol. Genet.* **16,** 515–528
9. Nessler, M., Puchala, J., Kwiatkowski, S., Kobylarz, K., Mojsa, I., and Chrapusta-Klimeczek, A. (2011) Multidisciplinary approach to the treatment of a patient with chondrodystrophic myotonia (Schwartz-Jampel vel Aberfeld Syndrome). *Ann. Plast. Surg.* **67,** 315–319
10. Costell, M., Gustafsson, E., Aszódi, A., Mörgelin, M., Bloch, W., Hunziker, E., Addicks, K., Timpl, R., and Fassler, R. (1999) Perlecan maintains the integrity of cartilage and some basement membranes. *J. Cell Biol.* **147,** 1109–1122
11. Stum, M., Girard, E., Bangratz, M., Bernard, V., Herbin, M., Vignaud, A., Ferry, A., Davoine, C. S., Echaniz-Laguna, A., René, F., Marcel, C., Molgó, J., Fontaine, B., Krejci, E., and Nicole, S. (2008) Evidence of a dosage effect and a physiological endplate acetylcholinesterase deficiency in the first mouse models mimicking Schwartz–Jampel syndrome neuromyotonia. *Hum. Mol. Genet.* **17,** 3166–3179
12. Martinez, J. R., Grindel, B. J., Hubka, K. M., Dodge, G. R., and Farach-Carson, M. C. (2019) Perlecan/HSPG2: Signaling role of domain IV in chondrocyte clustering with implications for Schwartz-Jampel Syndrome. *J. Cell. Biochem*. **120,** 2138–2150
13. Samsa, W. E., Zhou, X., and Zhou, G. (2017) Signaling pathways regulating cartilage growth plate formation and activity. *Semin. Cell Dev. Biol.* **62,** 3–15
14. Gubbiotti, M. A., Neill, T., and Iozzo, R. V. (2017) A current view of perlecan in physiology and pathology: A mosaic of functions. *Matrix Biol.* **57–58,** 285–298
15. Xu, X., Li, Z., Leng, Y., Neu, C. P., and Calve, S. (2016) Knockdown of the pericellular matrix molecule perlecan lowers in situ cell and matrix stiffness in developing cartilage. *Dev. Biol.* **418,** 242–247
16. Cescon, M., Gattazzo, F., Chen, P., and Bonaldo, P. (2015) Collagen VI at a glance. *J. Cell Sci.* **128,** 3525–3531
17. Han, L., Grodzinsky, A. J., and Ortiz, C. (2011) Nanomechanics of the cartilage extracellular matrix. *Annu. Rev. Mater. Res.* **41,** 133–168
18. Lycke, R. J., Walls, M. K., and Calve, S. (2019) Computational modeling of developing cartilage using experimentally derived geometries and compressive moduli. *J. Biomech. Eng.* **141,** 81002–81008
19. Long, F., and Linsenmayer, T. F. (1998) Regulation of growth region cartilage proliferation and differentiation by perichondrium. *Development* **125,** 1067–1073
20. Ishijima, M., Suzuki, N., Hozumi, K., Matsunobu, T., Kosaki, K., Kaneko, H, Hassell, J. R., Arikawa-Hirasawa, E., and Yamada, Y. (2012) Perlecan modulates VEGF signaling and is essential for vascularization in endochondral bone formation. *Matrix Biol.* **31,** 234–245
21. Naba, A., Clauser, K. R., Hoersch, S., Liu, H., Carr, S .A., and Hynes, R. O. (2012) The matrisome: in silico definition and in vivo characterization by proteomics of normal and tumor extracellular matrices. *Mol. Cell. Proteomics* **11**
22. Arikawa-Hirasawa, E., Watanabe, H., Takami, H., Hassell, J. R., and Yamada, Y. (1999) Perlecan is essential for cartilage and cephalic development. *Nat. Genet.* **23,** 354–358
23. Rueden, C. T., Schindelin, J., Hiner, M. C., DeZonia, B. E., Walter, A. E., Arena, E. T., and Eliceiri, K. W. (2017) ImageJ2: ImageJ for the next generation of scientific image data. *BMC Bioinformatics* **18,** 529
24. Schindelin, J., Arganda-Carreras, I., Frise, E., Kaynig, V., Longair, M., Pietzsch, T., Preibisch, S., Rueden, C., Saalfeld, S., Schmid, B., Tinevez, J. Y., White, D. J., Hartenstein, V., Eliceiri, K., Tomancak, P., and Cardona, A. (2012) Fiji: an open-source platform for biological-image analysis. *Nat. Methods* **9,** 676
25. Hoemann, C. D. (2004) Molecular and biochemical assays of cartilage components. *Methods Mol. Med.* **101,** 127–156
26. Hsueh, M. F., Khabut, A., Kjellström, S., Önnerfjord, P., and Kraus, V. B. (2016) Elucidating the molecular composition of cartilage by proteomics. *J. Proteome Res.* **15,** 374–388
27. Cox, J., and Mann, M. (2008) MaxQuant enables high peptide identification rates, individualized p.p.b.-range mass accuracies and proteome-wide protein quantification. *Nat. Biotechnol.* **26,** 1367
28. Naba, A., Pearce, O.M.T., Del Rosario, A., Ma, D., Ding, H., Rajeeve, V., Cutillas, P. R., Balkwill, F. R., and Hynes, R. O. (2017) Characterization of the extracellular matrix of normal and diseased tissues using proteomics. *J. Proteome Res.* **16,** 3083–3091
29. Ocken, A. R., Ku, M., Kinzer-Ursem, T. L., and Calve, S. (2019) Hspg2C1532YNeo DBA distal humeral cartilage proteomic comparison dataset. *MassIVE*
30. Reimand, J., Arak, T., Adler, P., Kolberg, L., Reisberg, S., Peterson, H., and Vilo, J. (2016) g:Profiler—a web server for functional interpretation of gene lists. (2016 update). *Nucleic Acids Res*. **44,** W83–W89
31. Starborg, T., Kalson, N. S., Lu, Y., Mironov, A., Cootes, T. F., Holmes, D. F., and Kadler, K. E. (2013) Using transmission electron microscopy and 3View to determine collagen fibril size and three-dimensional organization. *Nat. Protoc.* **8,** 1433
32. Wilson, R., Golub, S. B., Rowley, L., Angelucci, C., Karpievitch, Y. V., Bateman, J. F., and Fosang, A. J. (2016) Novel elements of the chondrocyte stress response identified using an in vitro model of mouse cartilage degradation. *J. Proteome Res.* **15,** 1033–1050
33. Ocken, A. R., Ku, M., Kinzer-Ursem, T. L., and Calve, S. (2019) Hspg2C1532YNeo DBA distal humeral cartilage secretome proteomic comparison. *MassIVE*
34. Jin, H., and Lewis, J. L. (2004) Determination of Poisson's ratio of articular cartilage by indentation using different-sized indenters. *J. Biomech. Eng.* **126,** 138–145
35. Trickey, W. R., Baaijens, F. P. T., Laursen, T. A., Alexopoulos, L. G., and Guilak, F. (2006) Determination of the Poisson's ratio of the cell: Recovery properties of chondrocytes after release from complete micropipette aspiration. *J. Biomech.* **39,** 78–87
36. Goeminne, L.J.E., Argentini, A., Martens, L., and Clement, L. (2015) Summarization vs peptide-based models in label-free quantitative proteomics: performance, pitfalls, and data analysis guidelines. *J. Proteome Res.* **14,** 2457–2465
37. Benjamini, Y., Krieger, A. M., and Yekutieli, D. (2006) Adaptive linear step-up procedures that control the false discovery rate. *Biometrika* **93,** 491–507
38. Hopf, M., Göhring, W., Kohfeldt, E., Yamada, Y., and Timpl, R. (1999) Recombinant domain IV of perlecan binds to nidogens, laminin-nidogen complex, fibronectin, fibulin-2 and heparin. *Eur. J. Biochem.* **259,** 917–926
39. Gomes, R., Kirn-Safran, C., Farach-Carson, M. C., and Carson, D. D. (2002) Perlecan: An important component of the cartilage pericellular matrix. *J. Musculoskelet. Neuronal Interact.* **2,** 511–516
40. Salmivirta, K., Talts, J. F., Olsson, M., Sasaki, T., Timpl, R., Ekblom, P. (2002) Binding of mouse nidogen-2 to basement membrane components and cells and its expression in embryonic and adult tissues suggest complementary functions of the two nidogens. *Exp. Cell Res.* **279,** 188–201
41. Shu, C. C., Smith, S. M., Little, C. B., and Melrose, J. (2019) Elevated hypertrophy, growth plate maturation, glycosaminoglycan deposition,

and exostosis formation in the Hspg2 exon 3 null mouse intervertebral disc. *Biochem. J.* **476,** 225–243
42. Cox, J., Hein, M. Y., Luber, C. A., Paron, I., Nagaraj, N., and Mann, M. (2014) Accurate proteome-wide label-free quantification by delayed normalization and maximal peptide ratio extraction, termed MaxLFQ. *Mol. Cell. Proteomics* **13,** 2513–2526
43. Saleh, A. M., Jacobson, K. R., Kinzer-Ursem, T. L., and Calve, S. (2019) Dynamics of non-canonical amino acid-labeled intra- and extracellular proteins in the developing mouse. *Cell Mol. Bioeng.* **12,** 495–509
44. Mi, H., Muruganujan, A., Ebert, D., Huang, X., and Thomas, P. D. (2018) PANTHER version 14: more genomes, a new PANTHER GO-slim and improvements in enrichment analysis tools. *Nucleic Acids Res.* **47,** D419–D426
45. Eyre, D. R., Brickley-Parsons, D. M., and Glimcher, M. J. (1978) Predominance of type I collagen at the surface of avian articular cartilage. *FEBS Lett.* **85,** 259–263
46. Kesava Reddy, G., and Enwemeka, C. S. (1996) A simplified method for the analysis of hydroxyproline in biological tissues. *Clin. Biochem.* **29,** 225–229
47. Berisio, R., Granata, V., Vitagliano, L., and Zagari, A. (2004) Imino acids and collagen triple helix stability: characterization of collagen-like polypeptides containing hyp-hyp-gly sequence repeats. *J. Am. Chem. Soc.* **126,** 11402–11403
48. Knott, L., and Bailey, A. J. (1998) Collagen cross-links in mineralizing tissues: A review of their chemistry, function, and clinical relevance. *Bone* **2,** 181–187
49. Kvist, A. J., Johnson, A. E., Mörgelin, M., Gustafsson, E., Bengtsson, E., Lindblom, K., Aszódi, A., Fässler, R., Sasaki, T., Timpl, R., and Aspberg, A. (2006) Chondroitin sulfate perlecan enhances collagen fibril formation: Implications for perlecan chondrodysplasias. *J. Biol. Chem.* **281,** 33127–33139
50. Gelse, K., Pöschl, E., and Aigner, T. (2003) Collagens-structure, function, and biosynthesis. *Adv. Drug Deliv. Rev.* **55,** 1531–1546
51. Fenton, J. I., Chlebek-Brown, K. A., Peters, T. L., Caron, J. P., and Orth, M. W. (2000) Glucosamine HCl reduces equine articular cartilage degradation in explant culture. *Osteoarthr. Cartil.* **8,** 258–265
52. Madsen, S. H., Goettrup, A. S., Thomsen, G., Christensen, S. T., Schultz, N., Henriksen, K., Bay-Jensen, A. C., and Karsdal, M. A. (2010) Characterization of an ex vivo femoral head model assessed by markers of bone and cartilage turnover. *Cartilage* **2,** 265–278
53. McCreery, K. P., Calve, S., and Neu, C. P. (2020) Ontogeny informs regeneration: explant models to investigate the role of the extracellular matrix in cartilage tissue assembly and development. *Connect. Tissue Res.* **61,** 1–14
54. Lorent, K, Overbergh, L, Delabie, J, Van Leuven, F, and Van den Berghe, H. (1994) Distribution of mRNA coding for Alpha-2-macroglobulin, the murinoglobulins, the Alpha-2-macroglobulin receptor and the Alpha-2-macroglobulin receptor associated protein during mouse embryogenesis and in adult tissues. *Differentiation* **55,** 213–223
55. Liu, B., Lad, N. K., Collins, A. T., Ganapathy, P. K., Utturkar, G. M., McNulty, A. L., Spritzer, C. E., Moorman, C. T., 3rd, Sutter, E. G., Garrett, W. E., and DeFrate, L. E. (2017) In vivo tibial cartilage strains in regions of cartilage-to-cartilage contact and cartilage-to-meniscus contact in response to walking. *Am. J. Sports Med.* **45,** 2817–2823
56. Anderson, D. E., and Johnstone, B. (2017) Dynamic mechanical compression of chondrocytes for tissue engineering: A critical review. *Front. Bioeng. Biotechnol.* **5,** 76
57. Wilson, R., Norris, E. L., Brachvogel, B., Angelucci, C., Zivkovic, S., Gordon, L., Bernardo, B. C., Stermann, J., Sekiguchi, K., Gorman, J. J., and Bateman, J. F. (2012) Changes in the chondrocyte and extracellular matrix proteome during post-natal mouse cartilage development. *Mol. Cell. Proteomics* **11,** 1296–1313
58. Boeuf, S., Steck, E., Pelttari, K., Hennig, T., Buneβ, A., Benz, K., Witte, D., Sültmann, H., Poustka, A., and Richter, W. (2008) Subtractive gene expression profiling of articular cartilage and mesenchymal stem cells: Serpins as cartilage-relevant differentiation markers. *Osteoarthr. Cartil.* **16,** 48–60
59. Iacobini, C., Fantauzzi, C. B., Pugliese, G., and Menini, S. (2017) Role of galectin-3 in bone cell differentiation, bone pathophysiology and vascular osteogenesis. *Int. J. Mol. Sci.* **18,** 2481
60. Blaschke, U. K., Eikenberry, E. F., Hulmes, D. J. S., Galla, H. J., and Bruckner, P. (2000) Collagen XI nucleates self-assembly and limits lateral growth of cartilage fibrils. *J. Biol. Chem.* **275,** 10370–10378
61. Heinegård, D., Lorenzo, P., Önnerfjord, P., and Saxne, T. (2015) Articular cartilage. In: Hochberg, M. C., Silman, A. J., Smolen, J. S., Weinblatt, M. E., Weisman, M. H. B. T. R. (Sixth E, editors. Rheumatology. 6th ed., Philadelphia: Mosby, p. 33–41
62. Tillgren, V., Ho, J. C. S., Önnerfjord, P., and Kalamajski, S. (2015) The novel small leucine-rich protein chondroadherin-like (CHADL) is expressed in cartilage and modulates chondrocyte differentiation. *J. Biol. Chem.* **290,** 918–925
63. Ishida, K., Acharya, C., Christiansen, B. A., Yik, J. H. N., DiCesare, P. E, and Haudenschild, D. R. (2013) Cartilage oligomeric matrix protein enhances osteogenesis by directly binding and activating bone morphogenetic protein-2. *Bone* **55,** 23–35
64. Bader, B. L., Smyth, N., Nedbal, S., Miosge, N., Baranowsky, A., Mokkapati, S., Murshed, M., and Nischt, R. (2005) Compound genetic ablation of nidogen 1 and 2 causes basement membrane defects and perinatal lethality in mice. *Mol. Cell. Biol.* **25,** 6846–6856
65. Miosge, N., Sasaki, T., and Timpl, R. (2002) Evidence of nidogen-2 compensation for nidogen-1 deficiency in transgenic mice. *Matrix Biol.* **21,** 611–621
66. Tashima, T., Nagatoishi, S., Sagara, H., Ohnuma, S., and Tsumoto, K. (2015) Osteomodulin regulates diameter and alters shape of collagen fibrils. *Biochem. Biophys. Res. Commun.* **463,** 292–296
67. Newman, B., Gigout, L. I., Sudre, L., Grant, M. E., and Wallis, G. A. (2001) Coordinated expression of matrix Gla protein is required during endochondral ossification for chondrocyte survival. *J. Cell Biol.* **154,** 659–666
68. Zelenski, N. A., Leddy, H. A., Sanchez-Adams, J., Zhang, J., Bonaldo, P., Liedtke, W., and Guilak, F. (2015) Type VI collagen regulates pericellular matrix properties, chondrocyte swelling, and mechanotransduction in mouse articular cartilage. *Arthritis Rheumatol.* **67,** 1286–1294
69. Plumb, D. A., Ferrara, L., Torbica, T., Knowles, L., Mironov Jr, Kadler, A. K. E., Briggs, M. D., and Boot-Handford, R. P. (2011) Collagen XXVII organises the pericellular matrix in the growth plate. *PLoS ONE* **6,** e29422
70. Almeida, P. C., Nantes, I. L., Chagas, J. R., Rizzi, C. C. A., Faljoni-Alario, A., Carmona, E., Juliano, L., Nader, H. B., and Tersariol, I. L. (2001) Cathepsin B activity regulation: heparin-like glycosaminoglycans protect human cathepsin B from alkaline pH-induced inactivation. *J. Biol. Chem.* **276,** 944–951
71. Turk, V., Stoka, V., Vasiljeva, O., Renko, M., Sun, T., Turk, B., and Turk, D. (2012) Cysteine cathepsins: From structure, function and regulation to new frontiers. *Biochim. Biophys. Acta* **1824,** 68–88
72. Flanagan-Steet, H., Christian, C., Lu, P. N., Aarnio-Peterson, M., Sanman, L., Archer-Hartmann, S., Azadi, P., Bogyo, M., and Steet, R. A. (2018) TGF-beta regulates cathepsin activation during normal and pathogenic development. *Cell Rep.* **22,** 2964–2977
73. Miedel, E. L., Brisson, B. K., Hamilton, T., Gleason, H., Swain, G. P., Lopas, L., Dopkin, D., Perosky, J. E., Kozloff, K. M., Hankenson, K. D., and Volk, S. W. (2015) Type III collagen modulates fracture callus bone formation and early remodeling. *J. Orthop. Res.* **33,** 675–684
74. Bland, Y. S., Critchlow, M. A., and Ashhurst, D. E. (1999) The expression of the fibrillar collagen genes during fracture healing: Heterogeneity of the matrices and differentiation of the osteoprogenitor cells. *Histochem. J.* **31,** 797–809
75. Okamura, N., Hasegawa, M., Nakoshi, Y., Iino, T., Sudo, A., Imanaka-Yoshida, K., Yoshida, T., and Uchida, A. (2010) Deficiency of tenascin-C delays articular cartilage repair in mice. *Osteoarthr. Cartil.* **18,** 839–848
76. Chijimatsu, R., Kunugiza, Y., Taniyama, Y., Nakamura, N., Tomita, T., and Yoshikawa, H. (2015) Expression and pathological effects of periostin in human osteoarthritis cartilage. *BMC Musculoskelet. Disord.* **16,** 215
77. Xu, X., Li, Z., Cai, L., Calve, S., and Neu, C. P. (2016) Mapping the nonreciprocal micromechanics of individual cells and the surrounding matrix within living tissues. *Sci. Rep.* **6,** 24272
78. Cao, L., Guilak, F., and Setton, L. A. (2009) Pericellular matrix mechanics in the anulus fibrosus predicted by a three-dimensional finite element model and in situ morphology. *Cell Mol. Bioeng.* **2,** 306–319
79. Cao, L., Guilak, F., and Setton, L. A. (2011) Three-dimensional finite element modeling of pericellular matrix and cell mechanics in the nucleus pulposus of the intervertebral disk based on in situ morphology. *Biomech. Model Mechanobiol.* **10,** 1–10
80. Guo, H., Maher, S. A., and Torzilli, P. A. (2014) A biphasic multiscale study of the mechanical microenvironment of chondrocytes within articular cartilage under unconfined compression. *J. Biomech.* **47,** 2721–2729